

Fourth- and higher-order finite element methods for the incompressible Navier-Stokes equations with Dirichlet boundary conditions

Yang Li^a, Heyu Wang^a, Qinghai Zhang^{a,b,*}

^a*School of Mathematical Sciences, Zhejiang University, Hangzhou, Zhejiang, 310058, China*

^b*Institute of Fundamental and Transdisciplinary Research, Zhejiang University, Hangzhou, Zhejiang, 310058, China*

Abstract

Inspired by the unconstrained pressure Poisson equation (PPE) formulation [Liu, Liu, & Pego, *Comm. Pure Appl. Math.* 60 (2007): 1443-1487], we previously proposed the generic projection and unconstrained PPE (GePUP) formulation [Zhang, *J. Sci. Comput.* 67 (2016): 1134-1180] for numerically solving the incompressible Navier-Stokes equations (INSE) with no-slip boundary conditions. In GePUP, the main evolutionary variable does not have to be solenoidal with its divergence controlled by a heat equation. This work presents high-order finite-element solvers for the INSE under the framework of method-of-lines. Continuous Lagrange finite elements of equal order are utilized for the velocity and pressure finite element spaces to discretize the weak form of GePUP in space, while high-order implicit-explicit Runge-Kutta methods are then employed to treat the stiff diffusion term implicitly and the other terms explicitly. Due to the implicit treatment of the diffusion term, the time step size is only restricted by convection. The solver is efficient in that advancing the solution at each time step only involves solving a sequence of linear systems either on the velocity or on the pressure with geometric multigrid methods. Furthermore, the solver is enhanced with adaptive mesh refinement so that the multiple length scales and time scales in flows at moderate or high Reynolds numbers can be efficiently resolved. Numerical tests with various Reynolds numbers are performed for the single-vortex test, the lid-driven cavity, and the flow past a cylinder/sphere, demonstrating the high-order accuracy of GePUP-FEM both in time and in space and its capability of accurately and efficiently capturing the right physics. Moreover, our solver offers the flexibility in choosing velocity and pressure finite element spaces and is free of the standard inf-sup condition.

Keywords: Incompressible Navier-Stokes equations, GePUP, Finite element method, Implicit-explicit Runge-Kutta method, Adaptive mesh refinement, Flow past a cylinder/sphere

1. Introduction

The Navier-Stokes equations (NSE) represent a fundamental set of equations governing the behavior of fluid flows and play a pivotal role in understanding a wide range of phenomena across various fields such as engineering, physics, meteorology, and biology. These equations, derived from the conservation laws of mass, momentum, and energy, describe the motion of viscous fluids under the influence of external forces. Understanding and solving the NSE are crucial for predicting the behavior of fluids in diverse scenarios, ranging from the airflow over an aircraft wing to the blood flow in human arteries. Moreover, these equations serve as the foundation for simulating and optimizing complex fluid dynamics problems encountered in practical engineering applications, including aerodynamics, hydrodynamics, heat transfer, and chemical engineering processes. Therefore, the development and application of efficient and accurate

*Corresponding author.

Email addresses: 3150104952@zju.edu.cn (Yang Li), wangheyu@zju.edu.cn (Heyu Wang), qinghai@zju.edu.cn (Qinghai Zhang)

numerical methods for solving the NSE not only advance our understanding of fluid mechanics, but also enable the design and optimization of innovative technologies that shape modern industries and enhance our everyday lives.

The incompressible Navier-Stokes equations (INSE) with Dirichlet boundary conditions read

$$\frac{\partial \mathbf{u}}{\partial t} + \mathbf{u} \cdot \nabla \mathbf{u} = \mathbf{f} - \nabla p + \nu \Delta \mathbf{u} \quad \text{in } \Omega, \quad (1a)$$

$$\nabla \cdot \mathbf{u} = 0 \quad \text{in } \Omega, \quad (1b)$$

$$\mathbf{u} = \mathbf{g} \quad \text{on } \partial\Omega, \quad (1c)$$

$$\mathbf{u}(\mathbf{x}, 0) = \mathbf{u}_0(\mathbf{x}) \quad \text{in } \Omega, \quad (1d)$$

where t is time, $\mathbf{x} \in \Omega \subset \mathbb{R}^D$ ($D = 2, 3$) is the spatial location, \mathbf{f} is the external forcing term, \mathbf{g} is the given velocity boundary function satisfying $\int_{\partial\Omega} \mathbf{g} \cdot \mathbf{n} = 0$, \mathbf{u}_0 is the given initial velocity field assumed to be divergence-free, \mathbf{u} is the velocity, p is the pressure, and ν is the kinematic viscosity.

As a fundamental and notoriously difficult problem, the well-posedness of the INSE (in \mathbb{R}^3 and $\mathbb{R}^3/\mathbb{Z}^3$ [1]) is selected by Smale [2] on his list of 18 mathematical problems for the 21st century and by the Clay Institute on the list of 7 millennium problems [3]. Since no one has solved this problem yet, numerical computation appears to be the only viable way for now to obtain approximate solutions of the INSE.

1.1. Challenges for the design of numerical solvers

In developing numerical methods for solving the INSE, we are confronted with four major challenges.

- (A) How to fulfill the divergence-free constraint (1b)?
- (B) How to achieve high-order accuracy both in time and in space?
- (C) How to accurately and efficiently capture structures of multiple length scales and time scales typically developed in flows with moderate or high Reynolds numbers?
- (D) How to decouple temporal integration from spatial discretization so that (i) the entire solver is constituted by orthogonal modules for these aspects, and (ii) solution methods for each aspect can be employed in a black-box manner and thus easily changed to make the entire solver versatile?

Challenge (A) concerns the special role of the pressure as a Lagrangian multiplier in enforcing the divergence-free constraint (1b). The lack of an evolution equation and suitable boundary conditions of the pressure makes it difficult to obtain high-order solutions for the pressure.

Challenges (B) and (C) concern accuracy and efficiency. A numerical method should resolve all scales that are relevant to the important physics. Compared with fourth- and higher-order methods, first- and second-order methods have simpler algorithms and cheaper computations, but towards a given accuracy the computational resources may be rapidly exhausted. It is shown both theoretically and analytically in [4, Section 7] that fourth-order methods may have a significant efficiency advantage over second-order methods. In fact, the speedup of high-order methods over low-order methods, as measured by the ratio of their CPU times, grows as a power function when the grid size or the targeted accuracy is reduced.

Challenge (B) also concerns faithful simulations of flows where velocity derivatives such as vorticity crucially affect the physics. For first-order methods, the computed velocity converges, but the vorticity does not, nor does the velocity gradient tensor. Consequently, the $O(1)$ error in the velocity gradient may lead to structures different from that of the original flow. Thus it is not clear whether solutions of a first-order method converge to the *right* physics. Similar suspicions apply to second-order methods for flows where second derivatives of the velocity are important. In particular, high-order accurate solvers are essential for simulating fluid-structure interaction problems, where accurate tractions are needed at fluid-solid interfaces.

Challenge (D) concerns versatility and user-friendliness of the numerical solver. To cater for the problem at hand, it is often desirable to change the time integrator from one to another. For example, flows with high viscosity are usually stiff while those with small viscosity are not; accordingly, an implicit time integrator should be used in the former case while an explicit one is usually suitable for the latter. If the internal details of a time integrator are rigidly coupled into the INSE solver, changing the time integrator would be

difficult and highly inconvenient. Hence a time integrator should be treated as a black box: for the ordinary differential equation (ODE) $\frac{d\mathbf{U}}{dt} = \mathbf{f}(\mathbf{U}, t)$, we should only need to feed into the time integrator the initial condition \mathbf{U}^n and samples of \mathbf{f} at a number of time instances to get the solution \mathbf{U}^{n+1} from the black box. The versatility further leads to user-friendliness. Analogous to an orthogonal basis of a vector space, the mutually independent policies span a space of solvers. In other words, each solver can be conveniently assembled by selecting a module for each constituting policy.

1.2. Some previous methods

1.2.1. Mixed finite element methods

Mixed finite element methods [5] tackle challenge (A) by treating both the velocity and the pressure simultaneously in an implicit fashion. For example, using the backward Euler method for time discretization and neglecting the nonlinear convection term, we are tasked with solving the following saddle-point problem at each time step: find $\mathbf{u}_h^{n+1} \in \mathbf{V}_h$ and $p_h^{n+1} \in Q_h$ such that

$$\forall \mathbf{v}_h \in \mathbf{V}_h, \quad \frac{1}{\Delta t}(\mathbf{u}_h^{n+1}, \mathbf{v}_h)_\Omega + \nu(\nabla \mathbf{u}_h^{n+1}, \nabla \mathbf{v}_h)_\Omega - (p_h^{n+1}, \nabla \cdot \mathbf{v}_h)_\Omega = \frac{1}{\Delta t}(\mathbf{u}_h^n, \mathbf{v}_h)_\Omega + (\mathbf{f}^{n+1}, \mathbf{v}_h)_\Omega, \quad (2a)$$

$$\forall q_h \in Q_h, \quad (q_h, \nabla \cdot \mathbf{u}_h^{n+1})_\Omega = 0, \quad (2b)$$

where \mathbf{V}_h and Q_h are the finite element spaces for the velocity and the pressure, respectively, Δt is the time step size, and $(\cdot, \cdot)_\Omega$ denotes the standard scalar-, vector-, or tensor-valued L^2 inner product defined on Ω .

Over the last fifty years, the mixed finite element methods have achieved tremendous successes and established elegant mathematical theories, the most significant of which is the inf-sup condition, also known as the Ladyzhenskaya-Babuška-Brezzi (LBB) condition,

$$\exists \beta > 0 \text{ s.t. } \forall h, \inf_{q_h \in Q_h} \sup_{\mathbf{v}_h \in \mathbf{V}_h} \frac{(q_h, \nabla \cdot \mathbf{v}_h)_\Omega}{\|q_h\|_{L^2(\Omega)} \|\mathbf{v}_h\|_{\mathbf{H}^1(\Omega)}} \geq \beta, \quad (3)$$

which is both sufficient and necessary for the well-posedness of the saddle-point problem (2). However, this condition limits the flexibility of the numerical methods as it is well known that equal-order Lagrange finite-element pairs for velocity and pressure approximations violate the inf-sup condition (3). Although it is possible to circumvent the inf-sup condition (3) by employing some stabilization techniques (such as continuous interior penalty [6] or subgrid-scale [7]) at the cost of additional complexity, developing efficient solution techniques for the saddle-point system (2) still poses significant challenges [8].

1.2.2. Projection methods

In stark contrast to the mixed finite element methods, the projection methods, pioneered by Chorin [9] and Temam [10], stand out for their high efficiency among various numerical methods for the INSE; they are based on the observation that the momentum equation (1a) can be rewritten as

$$\mathbf{a}^* = \mathbf{a} + \nabla p = \mathcal{P}\mathbf{a}^* + \nabla p, \quad (4)$$

where \mathbf{a} and \mathbf{a}^* are the *Eulerian accelerations* defined by

$$\mathbf{a} := \frac{\partial \mathbf{u}}{\partial t}, \quad \mathbf{a}^* := -\mathbf{u} \cdot \nabla \mathbf{u} + \mathbf{f} + \nu \Delta \mathbf{u}, \quad (5)$$

and \mathcal{P} is the Leray-Helmholtz projection operator defined by

$$\mathbf{v}^* = \mathcal{P}\mathbf{v}^* + \nabla \phi := \mathbf{v} + \nabla \phi,$$

where $\nabla \cdot \mathbf{v} = 0$ in Ω and $\mathbf{v} \cdot \mathbf{n}$ is given on $\partial\Omega$ and satisfies $\int_{\partial\Omega} \mathbf{v} \cdot \mathbf{n} = 0$.

In the original projection method independently proposed by Chorin [9] and Temam [10], the initial condition $\mathbf{u}^n \approx \mathbf{u}(t^n)$ is first advanced to an auxiliary velocity \mathbf{u}^* without worrying about the pressure gradient term and then \mathbf{u}^* is projected to the divergence-free space to obtain \mathbf{u}^{n+1} ,

$$\frac{\mathbf{u}^* - \mathbf{u}^n}{\Delta t} = -\mathbf{C}(\mathbf{u}^*, \mathbf{u}^n) + \mathbf{f}^n + \nu \mathbf{L} \mathbf{u}^*, \quad (6a)$$

$$\mathbf{u}^{n+1} = \mathbf{P} \mathbf{u}^*, \quad (6b)$$

where t^n is the starting time of the n th step, $\mathbf{f}^n = \mathbf{f}(t^n)$, $\mathbf{C}(\mathbf{u}^*, \mathbf{u}^n) \approx [\mathbf{u} \cdot \nabla \mathbf{u}](t^n)$, and \mathbf{L} and \mathbf{P} are discrete approximations of the Laplacian Δ and the Leray-Helmholtz projection \mathcal{P} , respectively. As a result, the INSE is advanced by solving a sequence of elliptic boundary value problems (BVPs) either on the velocity or on the pressure.

Chorin and Temam's original projection method (6) is only first-order accurate in time and its improvement to the second order has been the aim of many subsequent works, see the two excellent reviews [11, 12]. Moreover, there also exist many second-order adaptive projection methods in the literature, e.g., [13, 14, 15, 16].

A common basis of many second-order methods is the temporal discretization of the INSE (1) with the trapezoidal rule,

$$\frac{\mathbf{u}^{n+1} - \mathbf{u}^n}{\Delta t} + \nabla p^{n+\frac{1}{2}} = -[\mathbf{u} \cdot \nabla \mathbf{u}]^{n+\frac{1}{2}} + \mathbf{f}^{n+\frac{1}{2}} + \frac{\nu}{2} \Delta (\mathbf{u}^{n+1} + \mathbf{u}^n), \quad (7a)$$

$$\nabla \cdot \mathbf{u}^{n+1} = 0, \quad (7b)$$

where $p^{n+\frac{1}{2}} \approx p(t^{n+\frac{1}{2}})$, $\mathbf{f}^{n+\frac{1}{2}} = \mathbf{f}(t^{n+\frac{1}{2}})$, and $[\mathbf{u} \cdot \nabla \mathbf{u}]^{n+\frac{1}{2}} \approx [\mathbf{u} \cdot \nabla \mathbf{u}](t^{n+\frac{1}{2}})$ are numerical approximations at the mid-time $t^{n+\frac{1}{2}} = \frac{1}{2}(t^n + t^{n+1})$ of the n th step. Based on (7), many second-order projection methods with fractional stepping can be united [11] as follows,

- choose an auxiliary variable q and a boundary condition $\mathbf{B}(\mathbf{u}^*) = \mathbf{0}$ to solve for \mathbf{u}^* ,

$$\frac{\mathbf{u}^* - \mathbf{u}^n}{\Delta t} + \nabla q = -[\mathbf{u} \cdot \nabla \mathbf{u}]^{n+\frac{1}{2}} + \mathbf{f}^{n+\frac{1}{2}} + \frac{\nu}{2} \Delta (\mathbf{u}^* + \mathbf{u}^n); \quad (8)$$

- enforce (7b) with a discrete projection so that

$$\mathbf{u}^* = \mathbf{u}^{n+1} + \Delta t \nabla \phi^{n+1}; \quad (9)$$

- update the pressure by

$$p^{n+\frac{1}{2}} = q + U(\phi^{n+1}), \quad (10)$$

where the specific forms of q , $\mathbf{B}(\mathbf{u}^*)$, and $U(\phi^{n+1})$ vary from one method to another. Two examples are the method of Bell, Colella, and Glaz [17] specified by

$$q = p^{n-\frac{1}{2}}, \quad \mathbf{u}^*|_{\partial\Omega} = \mathbf{g}^{n+1}, \quad \nabla p^{n+\frac{1}{2}} = \nabla p^{n-\frac{1}{2}} + \nabla \phi^{n+1}, \quad (11)$$

and that of Kim and Moin [18] by

$$q = 0, \quad \mathbf{n} \cdot \mathbf{u}^*|_{\partial\Omega} = \mathbf{n} \cdot \mathbf{g}^{n+1}, \quad \boldsymbol{\tau} \cdot \mathbf{u}^*|_{\partial\Omega} = \boldsymbol{\tau} \cdot (\mathbf{g}^{n+1} + \Delta t \nabla \phi^n)|_{\partial\Omega}, \quad (12a)$$

$$\nabla p^{n+\frac{1}{2}} = \nabla \phi^{n+1} - \frac{\nu \Delta t}{2} \nabla \Delta \phi^{n+1}. \quad (12b)$$

As observed by Brown, Cortez, and Minion [11], the choices of q , $\mathbf{B}(\mathbf{u}^*)$, and $U(\phi^{n+1})$ are not independent. Indeed, substitute (9) into (8), subtract (7a), and we have

$$\nabla p^{n+\frac{1}{2}} = \nabla q + \nabla \phi^{n+1} - \frac{\nu \Delta t}{2} \Delta \nabla \phi^{n+1}. \quad (13)$$

Consequently, the pressure computed by (11) is only first-order accurate [11] because its pressure update formula is at an $O(\Delta t)$ discrepancy with (13). On the other hand, the pressure update formula (12b) complies with (13) due to the commutativity of the Laplacian and the gradient, but (12b) and (9) imply $p^{n+\frac{1}{2}} = \phi^{n+1} - \frac{\nu}{2} \nabla \cdot \mathbf{u}^*$, which may deteriorate the pressure accuracy to the first order [11]. Nonetheless, both methods (11) and (12) are second-order accurate for the velocity.

Projection methods have been successful. However, enhancing them to fourth- and higher-order accuracy presents a challenge. As discussed above, the choices of q , $\mathbf{B}(\mathbf{u}^*)$, and $U(\phi^{n+1})$ are coupled according to internal details of the time integrator. Consequently, switching from one time integrator to another calls for a new derivation. Furthermore, although appearing divorced, the velocity and the pressure are still implicitly coupled by the boundary condition of the auxiliary variable \mathbf{u}^* , with the coupling determined not by physics but still by internal details of the time integrator. Therefore, it is highly challenging, if not impossible, to answer challenges (B) and (D) via the approach of traditional projection methods.

1.3. The formulation of pressure Poisson equation (PPE)

The PPE describes an *instantaneous* relation between the pressure and the velocity in the INSE and, in domains with Dirichlet boundary conditions, has the form

$$\Delta p = \nabla \cdot (\mathbf{f} - \mathbf{u} \cdot \nabla \mathbf{u} + \nu \Delta \mathbf{u}) \quad \text{in } \Omega, \quad (14a)$$

$$\mathbf{n} \cdot \nabla p = \mathbf{n} \cdot \left(\mathbf{f} - \mathbf{u} \cdot \nabla \mathbf{u} + \nu \Delta \mathbf{u} - \frac{\partial \mathbf{g}}{\partial t} \right) \quad \text{on } \partial \Omega, \quad (14b)$$

where (14a) follows from the divergence of (1a) and the divergence-free condition (1b), while (14b) from the normal component of (1a) on $\partial \Omega$ and the Dirichlet boundary condition (1c). For the PPE in domains with other boundary conditions, (14b) should be replaced with the normal component of (4).

(1a), (1c), (14), and the additional boundary condition $\nabla \cdot \mathbf{u} = 0$ on $\partial \Omega$ are collectively called *the PPE formulation of the INSE with Dirichlet boundary conditions*, which is equivalent to the original INSE [19]. In terms of computation, however, the PPE formulation has a decisive advantage over the original INSE. If (1a) is discretized in time with (1b) as a constraint, the resulting index-2 differential algebraic system may suffer from large order reductions [20]. In contrast, replacing the divergence-free constraint with the PPE avoids this difficulty. As such, the PPE formulation allows the time integrator to be treated as a black box and thus to be easily changed; indeed, the pressure is an implicit function of \mathbf{u} and its interaction with \mathbf{u} is completely decoupled from internal details of the time integrator. Also, there is no need to introduce nonphysical auxiliary variables. These advantages of the PPE formulation have led to the development of numerous successful numerical methods. Two prominent examples are the unconstrained PPE formulation [21, 22, 23, 24, 25, 26] and the PPE formulation with electric boundary conditions [27, 28], which we briefly review in Sections 1.4 and 1.5, respectively. Earlier contributions include: Karniadakis et al. [29], who solved the PPE (14) by replacing the diffusion term $\nu \Delta \mathbf{u}$ in (14b) with $-\nu \nabla \times \nabla \times \mathbf{u}$ and employing a temporal extrapolation of the velocity field; Petersson [30], who investigated the stability properties of different pressure boundary conditions; and Leriche et al. [31], who proposed a non-splitting scheme by introducing an intermediate divergence-free acceleration field $\tilde{\mathbf{a}} = \partial \mathbf{u} / \partial t - \nu \Delta \mathbf{u}$. More recent contributions include: Li [32], who investigated accurate pressure boundary conditions at the discrete level; Meng et al. [33], who addressed complex moving domain problems using a WENO-based scheme on composite overlapping grids; and Pacheco et al. [34], who focused on simulating non-Newtonian incompressible flow problems.

Unfortunately, as observed by Liu, Liu, and Pego [22], (1a) and (14a) yield

$$\frac{\partial \nabla \cdot \mathbf{u}}{\partial t} = 0; \quad (15)$$

this degenerate equation implies that in the PPE formulation we have no control over $\nabla \cdot \mathbf{u}$ and its evolution is up to the particularities of the numerical schemes.

1.4. The formulation of unconstrained PPE (UPPE)

By applying the Leray-Helmholtz projection \mathcal{P} to (4), Liu, Liu, and Pego [22] obtained

$$\frac{\partial \mathbf{u}}{\partial t} - \mathcal{P}\mathbf{a}^* = \nu \nabla(\nabla \cdot \mathbf{u}), \quad (16)$$

where the zero right-hand side (RHS) is added for stability reasons. The divergence of (16) gives

$$\frac{\partial(\nabla \cdot \mathbf{u})}{\partial t} = \nu \Delta(\nabla \cdot \mathbf{u}), \quad (17)$$

which, together with the boundary condition $\nabla \cdot \mathbf{u} = 0$ on $\partial\Omega$, dictates an exponential decay of a nonzero $\nabla \cdot \mathbf{u}$ in Ω . A juxtaposition of (17) and (15) exposes a prominent advantage of (16) that any divergence residue caused by discretization errors is now well over control.

With the identity $\nabla(\nabla \cdot \mathbf{u}) = \Delta(\mathcal{I} - \mathcal{P})\mathbf{u}$ and the Laplace-Leray commutator $[\Delta, \mathcal{P}] := \Delta\mathcal{P} - \mathcal{P}\Delta$, Liu, Liu, and Pego [22] rewrote (16) as

$$\frac{\partial \mathbf{u}}{\partial t} + \mathcal{P}(\mathbf{u} \cdot \nabla \mathbf{u} - \mathbf{f}) + \nu[\Delta, \mathcal{P}]\mathbf{u} = \nu\Delta\mathbf{u}, \quad (18)$$

which provides a novel perspective on the INSE as a controlled perturbation of the vector diffusion equation $\frac{\partial \mathbf{u}}{\partial t} = \nu\Delta\mathbf{u}$. For a bounded and connected domain Ω with C^3 boundary, they established a sharp estimate on the L^2 -norm of the Laplace-Leray commutator $[\Delta, \mathcal{P}]\mathbf{u}$,

$$\forall \varepsilon > 0, \exists C \geq 0 \text{ s.t. } \forall \mathbf{u} \in \mathbf{H}^2(\Omega) \cap \mathbf{H}_0^1(\Omega), \int_{\Omega} |[\Delta, \mathcal{P}]\mathbf{u}|^2 \leq \left(\frac{1}{2} + \varepsilon\right) \int_{\Omega} |\Delta\mathbf{u}|^2 + C \int_{\Omega} |\nabla\mathbf{u}|^2 \quad (19)$$

and proved the unconditional stability and convergence of a first-order scheme without the standard inf-sup condition (3),

$$(\nabla p^n, \nabla \eta)_{\Omega} = (\mathbf{f}^n - \mathbf{u}^n \cdot \nabla \mathbf{u}^n + \nu\Delta\mathbf{u}^n - \nu\nabla\nabla \cdot \mathbf{u}^n, \nabla \eta)_{\Omega}, \quad (20a)$$

$$\frac{\mathbf{u}^{n+1} - \mathbf{u}^n}{\Delta t} - \nu\Delta\mathbf{u}^{n+1} = \mathbf{f}^n - \mathbf{u}^n \cdot \nabla \mathbf{u}^n - \nabla p^n \quad \text{in } \Omega, \quad (20b)$$

$$\mathbf{u}^{n+1} = \mathbf{0} \quad \text{on } \partial\Omega, \quad (20c)$$

where (20a) is the PPE in weak form with the test function $\eta \in H_{f=0}^1(\Omega) := \{\eta \in H^1(\Omega) : \int_{\Omega} \eta = 0\}$. For simplicity, (20) is presented for the case where the velocity satisfies homogeneous boundary conditions; nonhomogeneous conditions are discussed in [22].

In (20), the computations of pressure and velocity have been decoupled by treating the pressure gradient term explicitly and the viscous term implicitly. Its stability follows from (19) and the fact that the pressure gradient in the INSE consists of two parts:

$$\nabla p = \nabla p_c + \nu \nabla p_s, \quad \nabla p_c := (\mathcal{I} - \mathcal{P})(\mathbf{f} - \mathbf{u} \cdot \nabla \mathbf{u}), \quad \nabla p_s := [\Delta, \mathcal{P}]\mathbf{u},$$

where ∇p_c balances the divergence of the forcing term and the nonlinear convection term while ∇p_s accounts for the Laplace-Leray commutator. The stability and error estimates of the resulting fully discrete scheme with C^1 finite elements for velocity are further proved in [23], where the pair of velocity and pressure finite element spaces need not satisfy the inf-sup condition (3). This has also been observed for C^0 finite element schemes in numerical experiments [21, 25, 32].

From (18), Liu, Liu, and Pego [25] also deduced a strong form of the UPPE formulation as

$$\frac{\partial \mathbf{u}}{\partial t} + \mathbf{u} \cdot \nabla \mathbf{u} = \mathbf{f} - \nabla p + \nu\Delta\mathbf{u} \quad \text{in } \Omega, \quad (21a)$$

$$\mathbf{u} = \mathbf{g} \quad \text{on } \partial\Omega, \quad (21b)$$

$$\Delta p = \nabla \cdot (\mathbf{f} - \mathbf{u} \cdot \nabla \mathbf{u}) \quad \text{in } \Omega, \quad (21c)$$

$$\mathbf{n} \cdot \nabla p = \mathbf{n} \cdot \left(\mathbf{f} - \mathbf{u} \cdot \nabla \mathbf{u} - \nu \nabla \times \nabla \times \mathbf{u} - \frac{\partial \mathbf{g}}{\partial t} \right) \quad \text{on } \partial\Omega. \quad (21d)$$

Based on this formulation, they further devised improved approximations for the computation of pressure in existing pressure-approximation and pressure-update projection methods, and developed a slip-corrected projection method [25] that is third-order accurate in time for both velocity and pressure.

The PPE (14) and the UPPE (21c,d) have slightly different forms and nonetheless a crucial distinction: with the divergence of (21a), (21c) leads to (17) whereas (14a) leads to (15).

However, as discussed in [23, 24, 25], a straightforward finite-element discretization of the UPPE formulation (21) can lead to qualitatively incorrect results for problems where the solution is not sufficiently smooth, such as those with re-entrant corners. One possible remedy is to employ the Leray-Helmholtz projection operator \mathcal{P} to suppress the velocity divergence. However, \mathcal{P} is absent in (21) and thus any projection on the velocity in a method-of-lines (MOL) algorithm would be a mismatch of the numerical algorithm to the governing equations. Moreover, it is not clear which \mathbf{u} 's in (21) should be projected in MOL.

Another issue with the UPPE formulation (21) is that it is difficult for a discrete projection \mathbf{P} with fourth- or higher-order accuracy to satisfy properties of the Leray-Helmholtz projection \mathcal{P} , such as

$$\mathcal{P}^2 = \mathcal{P}, \quad \nabla \cdot \mathcal{P}\mathbf{v}^* = 0, \quad \mathcal{P}\nabla\phi = \mathbf{0}.$$

In particular, the discretely projected velocity might not be divergence-free. Then how does the approximation error of \mathbf{P} to \mathcal{P} affect the stability of the system of ODEs under the MOL framework? It is neither clear nor trivial how to answer this question with (21).

1.5. The PPE formulation with electric boundary conditions

To endow the heat equation (17) with homogeneous Dirichlet boundary conditions, Shirokoff and Rosales [27] proposed a novel PPE reformulation of the INSE, incorporating electric boundary conditions (EBC):

$$\frac{\partial \mathbf{u}}{\partial t} + \mathbf{u} \cdot \nabla \mathbf{u} = \mathbf{f} - \nabla p + \nu \Delta \mathbf{u} \quad \text{in } \Omega, \quad (22a)$$

$$\mathbf{n} \times \mathbf{u} = \mathbf{n} \times \mathbf{g}, \quad \nabla \cdot \mathbf{u} = 0 \quad \text{on } \partial\Omega, \quad (22b)$$

$$\Delta p = \nabla \cdot (\mathbf{f} - \mathbf{u} \cdot \nabla \mathbf{u}) \quad \text{in } \Omega, \quad (22c)$$

$$\mathbf{n} \cdot \nabla p = \mathbf{n} \cdot \left(\mathbf{f} - \mathbf{u} \cdot \nabla \mathbf{u} - \nu \nabla \times \nabla \times \mathbf{u} - \frac{\partial \mathbf{g}}{\partial t} \right) + \lambda \mathbf{n} \cdot (\mathbf{u} - \mathbf{g}) \quad \text{on } \partial\Omega, \quad (22d)$$

where (22b) is the EBC commonly encountered in electrostatics, and the term $\lambda \mathbf{n} \cdot (\mathbf{u} - \mathbf{g})$, with λ being a positive relaxation parameter, ensures that the normal velocity on the boundary decays exponentially.

To capture the structure imposed by the EBC (22b), Rosales et al. [28] introduced the vorticity $\boldsymbol{\omega} = \nabla \times \mathbf{u}$ as a new variable and employed mixed finite elements to solve for $\boldsymbol{\omega}$ and \mathbf{u} in space. However, this approach leads to a saddle-point problem, demanding that the finite element pair $(\boldsymbol{\omega}, \mathbf{u})$ satisfy the inf-sup condition. Moreover, this mixed formulation also increases the degrees of freedom (DoFs) in the discrete problem.

1.6. The contribution of this work

Inspired by the UPPE formulation (21), we previously proposed the generic projection and unconstrained PPE (GePUP) formulation [4] for solving the INSE with no-slip boundary conditions. This work is a continuation of [4] and our first step towards the development of high-order accurate finite-element solvers for simulating viscous incompressible flows. Specifically, we propose GePUP-FEM, INSE finite-element solvers that address all the challenges listed in Section 1.1. Novel features of GePUP-FEM include

- (i) *versatility*: time integration and spatial discretization are completely decoupled, so that high-order Runge-Kutta methods can be employed in a black-box manner;
- (ii) *accuracy*: fourth- and higher-order accuracy both in time and in space is achieved;
- (iii) *efficiency*: advancing the solution at each time step only involves solving a sequence of linear systems either on the velocity or on the pressure with geometric multigrid methods; moreover, GePUP-FEM is enhanced with adaptive mesh refinement to address Challenge (C);

(iv) *flexibility*: the choice of finite element spaces for the velocity and the pressure is free of the inf-sup condition (3).

To the best of our knowledge, GePUP-FEM is the first numerical method to possess all these features.

The rest of this paper is organized as follows. In Section 2, we briefly review the GePUP formulation of the INSE. In Section 3, we derive the weak form of the GePUP formulation and design high-order GePUP-FEM schemes via the method of lines. Benchmark problems are numerically solved in Section 4 to confirm the high-order accuracy of GePUP-FEM and its capability in accurately and efficiently capturing the right physics. Finally, Section 5 concludes this paper with some future research prospects.

2. The GePUP formulation

In numerically simulating incompressible flows, the computed velocity field rarely satisfies the divergence-free condition *exactly*. Correspondingly, we might as well relax the evolutionary variable to be slightly non-solenoidal while simultaneously setting up a mechanism to drive the divergence residue towards zero. More precisely, we perturb the divergence-free evolutionary variable \mathbf{u} in the time-derivative term to another velocity $\mathbf{w} := \mathbf{u} - \nabla\psi$ where ψ is some scalar function; meanwhile we change \mathbf{u} to \mathbf{w} in the diffusion term to set up the mechanism of divergence decay. Then there is no need to worry about the influence of $\nabla \cdot \mathbf{w} \neq 0$ on numerical stability because the evolution of \mathbf{w} is not subject to the divergence-free constraint. These ideas lead to the GePUP formulation proposed in [4], which we briefly review here for completeness.

2.1. The generic projection \mathcal{P}

A *generic projection* is a linear operator \mathcal{P} on a vector space satisfying

$$\mathcal{P}\mathbf{v}^* = \mathbf{v} := \mathbf{v}^* - \nabla\psi, \quad (23)$$

where ψ is a scalar function and $\nabla \cdot \mathbf{v} = 0$ may or may not hold. Since ψ is not specified in terms of \mathbf{v}^* , (23) is not a precise definition of \mathcal{P} , but rather a characterization of a family of operators, which, in particular, includes the Leray-Helmholtz projection \mathcal{P} . \mathcal{P} can be used to perturb the divergence-free velocity field \mathbf{u} to some non-solenoidal velocity $\mathbf{w} := \mathcal{P}\mathbf{u}$ and is thus more flexible than \mathcal{P} in characterizing discrete projections that fail to fulfill the divergence-free constraint exactly.

It follows from (23) and the commutativity of Δ and ∇ that

$$\Delta\mathcal{P} = \Delta - \nabla\nabla \cdot + \nabla\nabla \cdot \mathcal{P}. \quad (24)$$

2.2. GePUP: Reformulating INSE via generic projection and unconstrained PPE

To accommodate the fact that the discrete velocity field might not be divergence-free, the evolutionary variable of the GePUP formulation is designed to be a non-solenoidal velocity

$$\mathbf{w} := \mathcal{P}\mathbf{u} \quad (25)$$

instead of the divergence-free velocity \mathbf{u} in the UPPE formulation (21). The evolution of \mathbf{w} is governed by

$$\begin{aligned} \frac{\partial\mathbf{w}}{\partial t} &= \frac{\partial\mathcal{P}\mathbf{u}}{\partial t} = \mathcal{P}\frac{\partial\mathbf{u}}{\partial t} = \mathcal{P}\frac{\partial\mathbf{u}}{\partial t} - \nu(\Delta\mathbf{u} - \nabla\nabla \cdot \mathbf{u} + \nabla\nabla \cdot \mathcal{P}\mathbf{u} - \Delta\mathcal{P}\mathbf{u}) \\ &= \mathcal{P}\mathbf{a} - \mathbf{a}^* + \mathbf{f} - \mathbf{u} \cdot \nabla\mathbf{u} + \nu\nabla\nabla \cdot \mathbf{u} - \nu\nabla\nabla \cdot \mathbf{w} + \nu\Delta\mathbf{w} \\ &= \mathbf{f} - \mathbf{u} \cdot \nabla\mathbf{u} - \nabla q + \nu\Delta\mathbf{w}, \end{aligned}$$

where the first step follows from (25), the second from the commutativity of ∂_t and \mathcal{P} , the third from (24), the fourth from (25) and the definition of the Eulerian accelerations in (5), and the last from the definition

$$\nabla q := \mathbf{a}^* - \mathcal{P}\mathbf{a} - \nu\nabla\nabla \cdot \mathbf{u} + \nu\nabla\nabla \cdot \mathbf{w}. \quad (26)$$

The RHS of (26) is indeed a gradient field because of the decomposition in (4) and the definition in (23).

Although the projected velocity \mathbf{w} is allowed to be non-solenoidal, we demand

- (i) $\mathbf{w} = \mathbf{g}$ on $\partial\Omega$,
- (ii) its divergence $\nabla \cdot \mathbf{w}$ is governed by a heat equation with no-flux boundary conditions:

$$\frac{\partial(\nabla \cdot \mathbf{w})}{\partial t} = \nu \Delta(\nabla \cdot \mathbf{w}) \quad \text{in } \Omega, \quad (27a)$$

$$\mathbf{n} \cdot \nabla \nabla \cdot \mathbf{w} = 0 \quad \text{on } \partial\Omega. \quad (27b)$$

Consequently, we obtain *the GePUP formulation of the INSE with Dirichlet boundary conditions*

$$\frac{\partial \mathbf{w}}{\partial t} - \nu \Delta \mathbf{w} = \mathbf{f} - \mathbf{u} \cdot \nabla \mathbf{u} - \nabla q \quad \text{in } \Omega, \quad (28a)$$

$$\mathbf{w} = \mathbf{g} \quad \text{on } \partial\Omega, \quad (28b)$$

$$\mathbf{u} = \mathcal{P}\mathbf{w} \quad \text{in } \Omega, \quad (28c)$$

$$\mathbf{u} \cdot \mathbf{n} = \mathbf{g} \cdot \mathbf{n} \quad \text{on } \partial\Omega, \quad (28d)$$

$$\Delta q = \nabla \cdot (\mathbf{f} - \mathbf{u} \cdot \nabla \mathbf{u}) \quad \text{in } \Omega, \quad (28e)$$

$$\mathbf{n} \cdot \nabla q = \mathbf{n} \cdot \left(\mathbf{f} - \mathbf{u} \cdot \nabla \mathbf{u} - \nu \nabla \times \nabla \times \mathbf{u} - \frac{\partial \mathbf{g}}{\partial t} \right) \quad \text{on } \partial\Omega, \quad (28f)$$

where (28e) follows from the divergence of (26), (5), the commutativity of $\nabla \cdot$ and Δ , (25), and the assumption (27a), (28f) from the normal component of (26) on $\partial\Omega$, (5), the assumption (27b), and the identity

$$\Delta - \nabla \nabla \cdot = -\nabla \times \nabla \times. \quad (29)$$

Since the generic projection \mathcal{P} only perturbs the divergence-free velocity \mathbf{u} by a gradient field and any gradient field is in the null space of the Leray-Helmholtz projection \mathcal{P} , (28c) clearly holds.

Since (27a) is a starting point of our deriving GePUP from INSE, we expect that it can be recovered from (28). Indeed, the divergence of (28a) and (28e) yield (27a), which, together with the boundary condition (27b), drives $\nabla \cdot \mathbf{w}$ towards zero. Hence the GePUP formulation preserves the advantage of the UPPE formulation (21) that the velocity divergence decays exponentially.

Starting from the INSE, we obtain (28) as the consequence of (27) that dictates the exponential decay of $\nabla \cdot \mathbf{w}$. On the other hand, the INSE can be recovered from (28) by imposing the initial condition

$$\mathbf{w}(t_0) = \mathbf{u}(t_0) \quad \text{in } \bar{\Omega}, \quad (30)$$

where $\bar{\Omega}$ is the closure of Ω . (30) is natural because, designed as a perturbed version of \mathbf{u} , the non-solenoidal velocity \mathbf{w} should converge to \mathbf{u} . Therefore, *the GePUP formulation is equivalent to the INSE*.

We summarize prominent features of the GePUP formulation (28) as follows.

- (GPF-1) The sole evolutionary variable is the non-solenoidal velocity \mathbf{w} , with \mathbf{u} determined from \mathbf{w} via (28c,d) and q from \mathbf{u} via (28e,f). This chain of determination $\mathbf{w} \rightarrow \mathbf{u} \rightarrow q$ from Neumann BVPs is *instantaneous* and has nothing to do with time integration. Therefore, a time integrator in MOL can be employed in a black-box manner and thus may be easily changed without affecting other modules of the entire solver.
- (GPF-2) There is no ambiguity on which velocities should be projected and which should not in MOL.
- (GPF-3) Now that the main evolutionary variable is formally non-solenoidal, the Leray-Helmholtz projection \mathcal{P} only comes into the system (28) on the RHS. Although still contributing to the local truncation error, the approximation error of a discrete projection to \mathcal{P} does not affect numerical stability.

The two issues with the UPPE formulation (21) discussed in the last two paragraphs of Section 1.4 are resolved by (GPF-2) and (GPF-3).

3. GePUP-FEM

We develop high-order INSE solvers based on MOL, where the governing equations are first discretized in space by finite element methods and then a high-order time integrator is applied to the resulting system of ODEs. To this end, we first derive the weak form of the GePUP formulation (28).

3.1. The weak form of the GePUP formulation

Denote by $\mathbf{H}_{\mathbf{g}}^1(\Omega) := \{\mathbf{v} \in \mathbf{H}^1(\Omega) : \mathbf{v} = \mathbf{g} \text{ on } \partial\Omega\}$, multiply the GePUP formulation (28) by test functions, integrate by parts, and we obtain the following *weak form of the GePUP formulation* (28).

(i) advance the velocity \mathbf{w} by the momentum equation: find $\mathbf{w} \in L^2(0, T; \mathbf{H}_{\mathbf{g}}^1(\Omega))$ such that

$$\forall \mathbf{v} \in \mathbf{H}_{\mathbf{0}}^1(\Omega), \quad \left(\frac{\partial \mathbf{w}}{\partial t}, \mathbf{v} \right)_{\Omega} + \nu(\nabla \mathbf{w}, \nabla \mathbf{v})_{\Omega} = (\mathbf{f} - \mathbf{u} \cdot \nabla \mathbf{u} - \nabla q, \mathbf{v})_{\Omega}; \quad (31)$$

(ii) compute the divergence-free velocity \mathbf{u} : find $\phi \in H_{f=0}^1(\Omega)$ such that

$$\forall \eta \in H_{f=0}^1(\Omega), \quad (\nabla \phi, \nabla \eta)_{\Omega} = (\mathbf{w}, \nabla \eta)_{\Omega} - (\mathbf{n} \cdot \mathbf{g}, \eta)_{\partial\Omega}, \quad (32)$$

and set $\mathbf{u} = \mathbf{w} - \nabla \phi$;

(iii) extract the pressure q from the velocity \mathbf{u} : find $q \in H_{f=0}^1(\Omega)$ such that

$$\forall \eta \in H_{f=0}^1(\Omega), \quad (\nabla q, \nabla \eta)_{\Omega} = (\mathbf{f} - \mathbf{u} \cdot \nabla \mathbf{u}, \nabla \eta)_{\Omega} + \nu(\nabla \times \mathbf{u}, \mathbf{n} \times \nabla \eta)_{\partial\Omega} - \left(\mathbf{n} \cdot \frac{\partial \mathbf{g}}{\partial t}, \eta \right)_{\partial\Omega}. \quad (33)$$

The second term on the RHS of (33) is derived as follows.

$$\begin{aligned} (\mathbf{n} \cdot (\nabla \times \nabla \times \mathbf{u}), \eta)_{\partial\Omega} &= (\nabla \times \nabla \times \mathbf{u}, \nabla \eta)_{\Omega} = (\nabla \times \nabla \times \mathbf{u}, \nabla \eta)_{\Omega} - (\nabla \times \mathbf{u}, \nabla \times \nabla \eta)_{\Omega} \\ &= \int_{\Omega} \nabla \cdot ((\nabla \times \mathbf{u}) \times \nabla \eta) = \int_{\partial\Omega} \mathbf{n} \cdot ((\nabla \times \mathbf{u}) \times \nabla \eta) = -(\nabla \times \mathbf{u}, \mathbf{n} \times \nabla \eta)_{\partial\Omega}, \end{aligned}$$

where the first step follows from the divergence theorem and the identity (29), the second from the fact that the curl of any gradient field equals zero, the third from the vector identity

$$\nabla \cdot (\mathbf{F} \times \mathbf{G}) = (\nabla \times \mathbf{F}) \cdot \mathbf{G} - (\nabla \times \mathbf{G}) \cdot \mathbf{F},$$

the fourth from the divergence theorem, and the last from the vector identity

$$\mathbf{n} \cdot (\mathbf{F} \times \mathbf{G}) = -\mathbf{F} \cdot (\mathbf{n} \times \mathbf{G}).$$

Note that since the pressure is extracted by the weak form of an elliptic BVP, we require it to have the H^1 regularity. This differs from mixed formulations of the INSE, where the L^2 regularity suffices for the pressure.

3.2. Finite-element spatial discretization

Let \mathcal{T}_h be a mesh of the computational domain Ω with $h = \max_{K \in \mathcal{T}_h} h_K$, $\mathbf{V}_h \subset \mathbf{H}^1(\Omega)$ a space of C^0 finite elements for approximating the velocity field, $\mathbf{V}_{0,h} = \mathbf{V}_h \cap \mathbf{H}_0^1(\Omega)$ the subspace of \mathbf{V}_h consisting of vector fields that vanish on $\partial\Omega$, and $Q_h \subset H_{f=0}^1(\Omega)$ a space of C^0 finite elements for approximating the pressure field. For domains with curved boundaries, isoparametric finite elements are employed.

Because the pressure is explicitly determined by the Poisson equation (33), continuous Lagrange finite elements of equal order can be used for \mathbf{V}_h and Q_h . This contrasts with mixed finite element methods, where employing equal-order elements leads to instabilities due to the violation of the inf-sup condition (3).

Let $\{\eta_j\}_{j=1}^N$ be a basis of the continuous Lagrange finite element space and express the solutions as

$$\begin{aligned} \mathbf{w}_h(\mathbf{x}, t) &= \sum_{d=1}^D w_{h,d}(\mathbf{x}, t) \mathbf{e}_d, & w_{h,d}(\mathbf{x}, t) &= \sum_{j=1}^N w_{d,j}(t) \eta_j(\mathbf{x}), & \phi_h(\mathbf{x}, t) &= \sum_{j=1}^N \phi_j(t) \eta_j(\mathbf{x}), \\ \mathbf{u}_h(\mathbf{x}, t) &= \sum_{d=1}^D u_{h,d}(\mathbf{x}, t) \mathbf{e}_d, & u_{h,d}(\mathbf{x}, t) &= \sum_{j=1}^N u_{d,j}(t) \eta_j(\mathbf{x}), & q_h(\mathbf{x}, t) &= \sum_{j=1}^N q_j(t) \eta_j(\mathbf{x}), \end{aligned} \quad (34)$$

where the subscript d denotes a vector component, $\{\mathbf{e}_d\}_{d=1}^D$ is the standard basis of \mathbb{R}^D , $w_{d,j}(t), \phi_j(t), u_{d,j}(t)$, and $q_j(t)$ are the unknown coefficients to be sought. Restricting the weak formulations (31)–(33) to the finite-dimensional spaces $\mathbf{V}_{h,0}$ and Q_h and substituting (34) into the resulting equations, we obtain the following semi-discrete algorithm:

$$M \frac{d\mathbf{W}_{h,d}(t)}{dt} + \nu A \mathbf{W}_{h,d}(t) = \mathbf{F}_d^w(\mathbf{u}_h, q_h, \mathbf{f}), \quad (35a)$$

$$A \Phi_h = \mathbf{F}^\phi(\mathbf{w}_h, \mathbf{g}), \quad (35b)$$

$$M \mathbf{U}_{h,d} = \mathbf{F}_d^u(w_{h,d}, \phi_h), \quad (35c)$$

$$A \mathbf{Q}_h = \mathbf{F}^q(\mathbf{u}_h, \mathbf{f}, \mathbf{g}), \quad (35d)$$

where $\mathbf{W}_{h,d} \in \mathbb{R}^N$, $\Phi_h \in \mathbb{R}^N$, $\mathbf{U}_{h,d} \in \mathbb{R}^N$, and $\mathbf{Q}_h \in \mathbb{R}^N$ are the vectors with components $w_{d,j}(t)$, $\phi_j(t)$, $u_{d,j}(t)$, and $q_j(t)$, respectively, $M \in \mathbb{R}^{N \times N}$ and $A \in \mathbb{R}^{N \times N}$ are the mass and stiffness matrices, i.e., $m_{ij} = (\eta_i, \eta_j)_\Omega$ and $a_{ij} = (\nabla \eta_i, \nabla \eta_j)_\Omega$, and the i th components of the RHS of (35) are respectively

$$F_{d,i}^w(\mathbf{u}_h, q_h, \mathbf{f}) = \left(f_d - \mathbf{u}_h \cdot \nabla u_{h,d} - \frac{\partial q_h}{\partial x_d}, \eta_i \right)_\Omega, \quad (36a)$$

$$F_i^\phi(\mathbf{w}_h, \mathbf{g}) = (\mathbf{w}_h, \nabla \eta_i)_\Omega - (\mathbf{n} \cdot \mathbf{g}, \eta_i)_{\partial\Omega}, \quad (36b)$$

$$F_{d,i}^u(w_{h,d}, \phi_h) = \left(w_{h,d} - \frac{\partial \phi_h}{\partial x_d}, \eta_i \right)_\Omega, \quad (36c)$$

$$F_i^q(\mathbf{u}_h, \mathbf{f}, \mathbf{g}) = (\mathbf{f} - \mathbf{u}_h \cdot \nabla \mathbf{u}_h, \nabla \eta_i)_\Omega + \nu (\nabla \times \mathbf{u}_h, \mathbf{n} \times \nabla \eta_i)_{\partial\Omega} - \left(\mathbf{n} \cdot \frac{\partial \mathbf{g}}{\partial t}, \eta_i \right)_{\partial\Omega}, \quad (36d)$$

where the temporal derivative term $\frac{\partial \mathbf{g}}{\partial t}$ in (36d) can be computed using the analytic expression of the explicitly provided velocity Dirichlet boundary function $\mathbf{g}(\mathbf{x}, t)$.

3.3. Temporal integration

Besides the explicit treatment of the pressure gradient term to avoid solving large coupled saddle-point systems, it is also desirable for flows with low to moderate Reynolds numbers to treat the convection term explicitly and the diffusion term implicitly, because implicit treatment of the non-stiff convection term leads to a nonlinear system challenging for iterative solvers whereas explicit treatment of the stiff diffusion term incurs a stringent time step constraint. For this purpose, an implicit-explicit Runge-Kutta scheme [35] can be seamlessly integrated with the semi-discrete GePUP algorithm (35) to form a group of semi-implicit time-marching schemes for the INSE. In this work, we adopt two ERK-ESDIRK methods: one is the six-stage, fourth-order accurate ARK4(3)6L[2]SA scheme proposed in [36]; the other is the eight-stage, fifth-order accurate ARK5(4)8L[2]SA₂ scheme proposed in [37]. Both are L-stable and stiffly accurate.

For an ODE of the form

$$\frac{d\zeta}{dt} = \mathbf{X}^{[E]}(\zeta, t) + \mathbf{X}^{[I]}(\zeta),$$

the steps of an ERK-ESDIRK method are

$$\zeta^{(1)} = \zeta^n \approx \zeta(t^n), \quad (37a)$$

$$\forall s = 2, 3, \dots, n_s, \quad \left(I - \Delta t \gamma \mathbf{X}^{[I]} \right) \zeta^{(s)} = \zeta^n + \Delta t \sum_{j=1}^{s-1} a_{s,j}^{[E]} \mathbf{X}^{[E]} \left(\zeta^{(j)}, t^{(j)} \right) + \Delta t \sum_{j=1}^{s-1} a_{s,j}^{[I]} \mathbf{X}^{[I]} \left(\zeta^{(j)} \right), \quad (37b)$$

$$\zeta^{n+1} = \zeta^{(n_s)} + \Delta t \sum_{j=1}^{n_s} \left(b_j - a_{n_s,j}^{[E]} \right) \mathbf{X}^{[E]} \left(\zeta^{(j)}, t^{(j)} \right), \quad (37c)$$

where the superscript $^{(s)}$ denotes an intermediate stage, $t^{(s)} = t^n + c_s \Delta t$ the time of that stage, n_s the number of stages, $A^{[E]}$, \mathbf{b} and \mathbf{c} the coefficients of the Butcher tableau of the underlying ERK method, and

$A^{[I]}$, \mathbf{b} and \mathbf{c} those of the underlying ESDIRK method. Note that (37c) follows from

$$\zeta^{n+1} = \zeta^n + \Delta t \sum_{j=1}^{n_s} b_j^{[E]} \mathbf{X}^{[E]} \left(\zeta^{(j)}, t^{(j)} \right) + \Delta t \sum_{j=1}^{n_s} b_j^{[I]} \mathbf{X}^{[I]} \left(\zeta^{(j)} \right)$$

and $b_j^{[E]} = b_j^{[I]} = b_j = a_{r_{s,j}}^{[I]}$. For more details on this method, the reader is referred to [36, 37].

Applying the ERK-ESDIRK method (37) to the ODE system (35) with the splitting

$$\mathbf{X}^{[E]} := \mathbf{F}_d^w(\mathbf{u}_h, q_h, \mathbf{f}), \quad \mathbf{X}^{[I]} := -\nu A \mathbf{W}_{h,d}$$

yields the following fully discrete GePUP-FEM algorithm:

$$\mathbf{W}_{h,d}^{(1)} = \mathbf{W}_{h,d}^n, \quad (38a)$$

$$\forall s = 2, 3, \dots, n_s, \quad \left\{ \begin{array}{l} (M + \nu \Delta t \gamma A) \mathbf{W}_{h,d}^{(s)} = M \mathbf{W}_{h,d}^n + \Delta t \sum_{j=1}^{s-1} a_{s,j}^{[E]} \mathbf{F}_d^w \left(\mathbf{u}_h^{(j)}, q_h^{(j)}, \mathbf{f}^{(j)} \right) + \nu \Delta t \sum_{j=1}^{s-1} a_{s,j}^{[I]} A \mathbf{W}_{h,d}^{(j)}, \\ A \Phi_h^{(s)} = \mathbf{F}^\phi \left(\mathbf{w}_h^{(s)}, \mathbf{g}^{(s)} \right), \\ M \mathbf{U}_{h,d}^{(s)} = \mathbf{F}_d^u \left(w_{h,d}^{(s)}, \phi_h^{(s)} \right), \\ A \mathbf{Q}_h^{(s)} = \mathbf{F}^q \left(\mathbf{u}_h^{(s)}, \mathbf{f}^{(s)}, \mathbf{g}^{(s)} \right), \end{array} \right. \quad (38b)$$

$$\left\{ \begin{array}{l} M \mathbf{W}_{h,d}^* = M \mathbf{W}_{h,d}^{(n_s)} + \Delta t \sum_{j=1}^{n_s} \left(b_j - a_{n_s,j}^{[E]} \right) \mathbf{F}_d^w \left(\mathbf{u}_h^{(j)}, q_h^{(j)}, \mathbf{f}^{(j)} \right), \\ A \Phi_h^{n+1} = \mathbf{F}^\phi \left(\mathbf{w}_h^*, \mathbf{g}^{n+1} \right), \\ M \mathbf{U}_{h,d}^{n+1} = \mathbf{F}_d^u \left(w_{h,d}^*, \phi_h^{n+1} \right), \\ A \mathbf{Q}_h^{n+1} = \mathbf{F}^q \left(\mathbf{u}_h^{n+1}, \mathbf{f}^{n+1}, \mathbf{g}^{n+1} \right), \\ \mathbf{W}_{h,d}^{n+1} = \mathbf{U}_{h,d}^{n+1}. \end{array} \right. \quad (38c)$$

Due to the nonlinear convection term in $\mathbf{X}^{[E]}$, the divergence of \mathbf{w}_h^* in (38c) is much greater than that of $\mathbf{w}_h^{(s)}$ in previous stages. Hence, the final solution \mathbf{w}_h^{n+1} of this time step is set to \mathbf{u}_h^{n+1} , not \mathbf{w}_h^* .

In summary, our numerical algorithms are

- versatile: time integrators can be employed in a black-box manner;
- accurate: fourth- and higher-order accuracy both in time and in space is achieved;
- efficient: at each time step, advancing the INSE amounts to solving a sequence of elliptic BVPs, for which highly efficient linear solvers are readily available;
- flexible: the selected finite element spaces for the velocity and the pressure do not have to satisfy the inf-sup condition (3).

4. Numerical tests

In this section, we test GePUP-FEM by standard benchmark problems to demonstrate its fourth- and higher-order accuracy and its capability of accurately and efficiently resolving the right physics. Our numerical algorithm is implemented using the state-of-the-art open-source C++ finite element library `deal.II` [38], which supports distributed quadrilateral/hexahedral meshes via `p4est` [39], matrix-free computations with sum factorization [40], and adaptive mesh refinement (AMR) with hanging nodes [41]. The resulting linear

Table 1: Errors and convergence rates of the fourth-order GePUP-FEM scheme for the Taylor-Green vortex with $\text{Re} = 100$, $t_0 = 0.0$, $t_e = 1.0$, and $\text{Cr} = 0.8$.

	$h = \frac{1}{8}$	Rate	$h = \frac{1}{16}$	Rate	$h = \frac{1}{32}$	Rate	$h = \frac{1}{64}$	
\mathbf{L}^2	9.28e-06	4.65	3.69e-07	4.43	1.71e-08	4.19	9.38e-10	
\mathbf{u}	\mathbf{H}^1	8.47e-04	3.44	7.80e-05	3.15	8.77e-06	3.04	1.07e-06
\mathbf{L}^∞		4.19e-05	4.47	1.89e-06	4.24	9.97e-08	4.17	5.53e-09
L^2		1.68e-05	4.03	1.03e-06	4.02	6.36e-08	4.01	3.95e-09
q	H^1	1.64e-03	3.01	2.03e-04	3.00	2.54e-05	3.00	3.17e-06
L^∞		5.57e-05	3.94	3.62e-06	3.99	2.29e-07	3.97	1.46e-08

systems are solved by the conjugate gradient method preconditioned by geometric multigrid [42]. All our numerical simulations were performed on a server with AMD Ryzen Threadripper PRO 3995WX 64-Core CPUs running at 2.70 GHz.

As discussed in the previous section, we employ continuous Lagrange finite elements of equal order for the velocity and pressure finite element spaces which are known to violate the inf-sup condition (3). The time step size Δt is determined by the Courant number

$$\text{Cr} := k\Delta t \max_{K \in \mathcal{T}_h} \frac{\|\mathbf{u}_h\|_{\mathbf{L}^\infty(K)}}{h_K}, \quad (39)$$

where k is the polynomial degree of the employed Lagrange finite element.

4.1. Numerical tests for convergence rates

In this subsection, standard benchmark problems are solved to verify the high-order accuracy of GePUP-FEM both in time and in space. We test two combinations: one is a fourth-order GePUP-FEM scheme with ARK4(3)6L[2]SA as the time integrator and continuous \mathbb{Q}_3 -elements for both the velocity and pressure finite element spaces; the other is a fifth-order GePUP-FEM scheme with ARK5(4)8L[2]SA₂ as the time integrator and continuous \mathbb{Q}_4 -elements for both the velocity and pressure finite element spaces.

4.1.1. Taylor-Green vortex in two dimensions

This test concerns the two-dimensional Taylor-Green vortex [43, 44] with analytic solutions

$$\mathbf{u}(x, y, t) = e^{-\frac{2\pi^2 t}{\text{Re}}} \begin{pmatrix} -\cos(\pi x) \sin(\pi y) \\ \sin(\pi x) \cos(\pi y) \end{pmatrix}, \quad (40a)$$

$$p(x, y, t) = -\frac{1}{4} e^{-\frac{4\pi^2 t}{\text{Re}}} (\cos(2\pi x) + \cos(2\pi y)), \quad (40b)$$

where $\text{Re} = 1/\nu$ is the Reynolds number. The time derivative of the velocity cancels the diffusion term and the pressure gradient cancels the convection term, resulting in a zero external force. The Dirichlet boundary condition for the velocity is taken as the restriction of the exact solution to the domain boundary and the initial condition as an instantiation of the exact solution at t_0 .

In the unit square $\Omega = (0, 1)^2$, (40) is advanced from $t_0 = 0$ to $t_e = 1$ with $\text{Cr} = 0.8$ on four successively refined square grids with size h . Errors and convergence rates of the fourth- and fifth-order GePUP-FEM schemes for $\text{Re} = 100$ are summarized in Tables 1 and 2, respectively, which clearly show the expected convergence rates for both the velocity and the pressure, i.e., for the k th-order GePUP-FEM scheme, both the velocity and the pressure are k th-order accurate in the L^2 - and L^∞ -norms and $(k-1)$ th-order accurate in the H^1 -norm.

Table 2: Errors and convergence rates of the fifth-order GePUP-FEM scheme for the Taylor-Green vortex with $\text{Re} = 100$, $t_0 = 0.0$, $t_e = 1.0$, and $\text{Cr} = 0.8$.

	$h = \frac{1}{8}$	Rate	$h = \frac{1}{16}$	Rate	$h = \frac{1}{32}$	Rate	$h = \frac{1}{64}$	
\mathbf{L}^2	3.90e-07	5.73	7.35e-09	5.67	1.44e-10	5.47	3.26e-12	
\mathbf{u}	\mathbf{H}^1	5.66e-05	4.70	2.18e-06	4.69	8.46e-08	4.50	3.74e-09
	\mathbf{L}^∞	1.24e-06	5.61	2.53e-08	5.69	4.88e-10	5.55	1.04e-11
q	L^2	6.56e-07	4.97	2.09e-08	4.83	7.37e-10	4.54	3.16e-11
	H^1	8.29e-05	4.03	5.06e-06	4.01	3.13e-07	4.00	1.95e-08
	L^∞	2.34e-06	4.92	7.71e-08	4.97	2.47e-09	4.79	8.91e-11

4.1.2. Beltrami flow in three dimensions

In this test, we consider the three-dimensional Beltrami flow [45, 46] with exact solutions

$$\mathbf{u}(x, y, z, t) = -ae^{-\frac{d^2t}{\text{Re}}} \begin{pmatrix} e^{ax} \sin(ay + dz) + e^{az} \cos(ax + dy) \\ e^{ay} \sin(az + dx) + e^{ax} \cos(ay + dz) \\ e^{az} \sin(ax + dy) + e^{ay} \cos(az + dx) \end{pmatrix}, \quad (41a)$$

$$p(x, y, z, t) = -\frac{a^2}{2} e^{-\frac{2d^2t}{\text{Re}}} \left(e^{2ax} + e^{2ay} + e^{2az} + 2 \sin(ax + dy) \cos(az + dx) e^{a(y+z)} + 2 \sin(ay + dz) \cos(ax + dy) e^{a(z+x)} + 2a \sin(az + dx) \cos(ay + dz) e^{a(x+y)} \right), \quad (41b)$$

where $\text{Re} = 1/\nu$ is the Reynolds number, $a = \pi/4$, and $b = \pi/2$. As in Section 4.1.1, the time derivative of the velocity cancels the diffusion term and the pressure gradient cancels the convection term, resulting in a zero forcing term. The Dirichlet boundary condition for the velocity is taken as the restriction of the exact solution to the domain boundary and the initial condition as an instantiation of the exact solution at t_0 .

In the cube $\Omega = (-1, 1)^3$, (41) is advanced from $t_0 = 0$ to $t_e = 1$ with $\text{Cr} = 0.4$ on four successively refined uniform hexahedral meshes with element side length h . Errors and convergence rates of the fourth- and fifth-order GePUP-FEM schemes for $\text{Re} = 100$ are presented in Tables 3 and 4, respectively. It is observed that while the velocity exhibits the expected convergence rates in all norms, the pressure has order reductions in the L^2 - and L^∞ -norms. These order reductions may be caused by the evaluation of the term $(\nabla \times \mathbf{u}_h, \mathbf{n} \times \nabla \eta_i)_{\partial\Omega}$ in (36d) and the fact that the direct evaluation of $\nabla \times \mathbf{u}_h$ from the finite element solution \mathbf{u}_h is of sub-optimal order of accuracy. However, we see that the convergence rate of the pressure in the H^1 -norm is as expected.

To demonstrate the efficiency advantage of GePUP-FEM, we compare it with a second-order consistent splitting (CS) scheme [12] by their running times in achieving the same accuracy. For this comparison, we implemented the CS scheme using a second-order implicit-explicit Runge-Kutta method [35] as the time integrator and continuous Q_1 -elements for both the velocity and pressure finite element spaces. Errors and convergence rates of this second-order CS scheme are shown in Table 5. The CPU times (in seconds) for the second-order CS scheme are 0.22, 1.85, 24.73, and 307.53 on the four successively refined meshes, while those for the fourth-order GePUP-FEM scheme are 5.04, 15.92, 101.16, and 1258.68. The \mathbf{L}^2 -norm of the velocity error of the fourth-order GePUP-FEM scheme with $h = 2^{-2}$ is 4.05×10^{-5} while that of the second-order CS scheme with $h = 2^{-4}$ is 5.10×10^{-3} . For the second-order CS scheme to achieve the same accuracy 4.05×10^{-5} of the fourth-order GePUP-FEM scheme, even with an optimal complexity of solving linear systems, the mesh has to be refined at least $\log_{2^2} \frac{5.10 \times 10^{-3}}{4.05 \times 10^{-5}} \approx 3.49$ times, resulting in a running time of at least $307.53 \times (2^3 \times 2)^{3.49} \approx 4.9 \times 10^6$ seconds, where the “ $\times 2$ ” comes from the fact that the time step size is also halved during mesh refinement. Thus, the speedup of the fourth-order GePUP-FEM scheme over the second-order CS scheme in achieving a velocity \mathbf{L}^2 accuracy of 4.05×10^{-5} is $4.9 \times 10^6 / 15.92 \approx 3.08 \times 10^5$! This clearly illustrates the efficiency advantage of the high-order accurate GePUP-FEM schemes.

Table 3: Errors and convergence rates of the fourth-order GePUP-FEM scheme for the Beltrami flow with $\text{Re} = 100$, $t_0 = 0.0$, $t_e = 1.0$, and $\text{Cr} = 0.4$.

	$h = \frac{1}{2}$	Rate	$h = \frac{1}{4}$	Rate	$h = \frac{1}{8}$	Rate	$h = \frac{1}{16}$	
\mathbf{L}^2	8.91e-04	4.46	4.05e-05	4.12	2.32e-06	4.16	1.30e-07	
\mathbf{u}	\mathbf{H}^1	1.76e-02	3.37	1.70e-03	3.12	1.96e-04	3.08	2.32e-05
	\mathbf{L}^∞	1.12e-03	4.41	5.27e-05	4.12	3.03e-06	4.08	1.79e-07
\mathbf{L}^2	1.00e-03	4.14	5.68e-05	3.89	3.84e-06	3.61	3.16e-07	
q	\mathbf{H}^1	1.99e-02	3.13	2.28e-03	3.02	2.81e-04	3.01	3.49e-05
	\mathbf{L}^∞	1.93e-03	3.29	1.98e-04	3.59	1.64e-05	3.62	1.33e-06

Table 4: Errors and convergence rates of the fifth-order GePUP-FEM scheme for the Beltrami flow with $\text{Re} = 100$, $t_0 = 0.0$, $t_e = 1.0$, and $\text{Cr} = 0.4$.

	$h = \frac{1}{2}$	Rate	$h = \frac{1}{4}$	Rate	$h = \frac{1}{8}$	Rate	$h = \frac{1}{16}$	
\mathbf{L}^2	6.13e-05	5.15	1.73e-06	5.65	3.44e-08	5.63	6.93e-10	
\mathbf{u}	\mathbf{H}^1	1.80e-03	4.17	1.00e-04	4.59	4.16e-06	4.53	1.80e-07
	\mathbf{L}^∞	9.45e-05	4.84	3.30e-06	5.50	7.31e-08	4.66	2.88e-09
\mathbf{L}^2	7.70e-05	4.87	2.63e-06	5.02	8.15e-08	4.66	3.21e-09	
q	\mathbf{H}^1	2.41e-03	4.09	1.41e-04	4.39	6.74e-06	4.26	3.53e-07
	\mathbf{L}^∞	2.03e-04	4.55	8.66e-06	4.02	5.36e-07	3.90	3.58e-08

Table 5: Errors and convergence rates of a second-order consistent splitting scheme [12] for the Beltrami flow with $\text{Re} = 100$, $t_0 = 0.0$, $t_e = 1.0$, and $\text{Cr} = 0.4$.

	$h = \frac{1}{2}$	Rate	$h = \frac{1}{4}$	Rate	$h = \frac{1}{8}$	Rate	$h = \frac{1}{16}$	
\mathbf{L}^2	3.33e-01	1.97	8.47e-02	2.03	2.07e-02	2.02	5.10e-03	
\mathbf{u}	\mathbf{H}^1	1.98e+00	1.14	8.99e-01	1.06	4.33e-01	1.02	2.14e-01
	\mathbf{L}^∞	2.34e-01	1.89	6.34e-02	2.07	1.51e-02	2.09	3.54e-03
\mathbf{L}^2	5.41e-01	1.87	1.47e-01	1.98	3.75e-02	1.97	9.59e-03	
p	\mathbf{H}^1	2.04e+00	1.23	8.68e-01	1.10	4.06e-01	1.03	1.99e-01
	\mathbf{L}^∞	6.52e-01	1.10	3.05e-01	1.68	9.50e-02	1.78	2.77e-02

4.2. Acceptance tests via physical benchmarks

In this subsection, standard benchmark problems, including a single-vortex test, a lid-driven cavity, two-dimensional flows past a circular cylinder, and three-dimensional flows past a sphere, are simulated to demonstrate that GePUP-FEM is capable of accurately and efficiently resolving the right physics, i.e., *converging to the correct solution*. We only test the fourth-order GePUP-FEM, i.e., ARK4(3)6L[2]SA as the time integrator and continuous (isoparametric) \mathbb{Q}_3 -elements for both the velocity and pressure finite element spaces.

To efficiently resolve strongly localized features, we augment GePUP-FEM to support adaptive mesh refinement via the steps **SOLVE** → **ESTIMATE** → **MARK** → **REFINE**. In the **ESTIMATE** step, we calculate the indicator of local refinement by

$$\forall K \in \mathcal{T}_h, \quad \eta_K = h_K \|\nabla \times \mathbf{u}_h\|_{\mathbf{L}^\infty(K)}.$$

In the **MARK** step, the Dörfler marking strategy [47] is employed to mark the set \mathcal{R}_h of all refined elements and the set \mathcal{C}_h of all coarsened elements as

$$\text{find } \mathcal{R}_h \subset \mathcal{T}_h \text{ s.t. } \sum_{K \in \mathcal{R}_h} \eta_K \geq \theta_R \sum_{K \in \mathcal{T}_h} \eta_K \text{ with minimal cardinality,} \quad (42a)$$

$$\text{find } \mathcal{C}_h \subset \mathcal{T}_h \text{ s.t. } \sum_{K \in \mathcal{C}_h} \eta_K \leq \theta_C \sum_{K \in \mathcal{T}_h} \eta_K \text{ with maximal cardinality,} \quad (42b)$$

where $\theta_R \in (0, 1)$ and $\theta_C \in (0, 1)$ are the refining threshold and the coarsening threshold, respectively. The Dörfler marking strategy (42) is known [48] to have optimal complexity. For more details on the algorithms and data structures for massively parallel adaptive finite element codes, the reader is referred to [41].

4.2.1. Single vortex

While the tests in Section 4.1 focus on the high-order accuracy of our numerical solver, the purpose of this test is to illustrate its efficiency in accurately capturing sharp gradients and localized features near the boundaries, which are characteristic of boundary layer-like structures in this 2D example. Following [49], we consider an axisymmetric velocity field defined on the unit square $(0, 1)^2$ by

$$u_\theta(r_v) = \begin{cases} \frac{1}{2}r_v - 4r_v^3 & \text{if } r_v < R; \\ \frac{R}{r_v} \left(\frac{1}{2}R - 4R^3 \right) & \text{if } r_v \geq R, \end{cases}$$

where r_v is the distance from (x, y) to the vortex center $(0.5, 0.5)$ and $R = 0.2$. Before being used as the initial condition of the INSE, this non-solenoidal vector field is projected by the discrete Leray-Helmholtz projection operator so that it is approximately divergence-free. The velocity satisfies no-slip boundary conditions $\mathbf{u} = \mathbf{0}$ on the whole domain boundary. The external forcing function \mathbf{f} is taken to be zero. The kinematic viscosity ν is chosen so that the Reynolds number $\text{Re} = LU_\infty/\nu$ is either 2×10^4 or 10^5 , where $L = 1$ is the side length of the unit square and $U_\infty = \max(u_\theta) = 0.068$ is the maximal velocity magnitude.

The time span $[0, 60]$ is made long enough for the turbulent boundary layers to develop prominent Lagrangian coherent structures. The tests are performed using both AMR and single-level meshes. In the case of single-level meshes, uniform square grids with size $h = 2^{-9}$ and $h = 2^{-10}$ are used for $\text{Re} = 2 \times 10^4$ and $\text{Re} = 10^5$, respectively. In the case of AMR, the number of refinements of the unit square $(0, 1)^2$ is allowed to vary between 6 and 9 for $\text{Re} = 2 \times 10^4$, and between 7 and 10 for $\text{Re} = 10^5$. Since we are only interested in regions near the domain boundaries, the number of refinements within the disk of radius 0.2 centered at the vortex center is limited to 7 and 8 for $\text{Re} = 2 \times 10^4$ and $\text{Re} = 10^5$, respectively. After every 50 time steps, we adaptively refine and coarsen the mesh and adjust the time step size, where the thresholds for refinement and coarsening in the Dörfler marking strategy (42) are $\theta_R = 0.6$ ($\text{Re} = 2 \times 10^4$), $\theta_R = 0.8$ ($\text{Re} = 10^5$), and $\theta_C = 0.1$. The time step size is adjusted by (39) and $\text{Cr} = 0.8$.

Figure 1 shows snapshots of the vorticity field at $t_e = 60$. The essential features of vortex sheet roll-up and counter-vortices agree well with those in [49]. In terms of the coherent structures, there is no observable

Table 6: Performance comparison between AMR and single-level meshes for the single-vortex test at $Re = 2 \times 10^4$ and $Re = 10^5$. The single level is discretized by square grids with size $h = 2^{-9}$ ($Re = 2 \times 10^4$) and $h = 2^{-10}$ ($Re = 10^5$). The AMR hierarchy contains four levels with h varying between 2^{-9} and 2^{-6} for $Re = 2 \times 10^4$, and between 2^{-10} and 2^{-7} for $Re = 10^5$. The simulations were performed on a server with AMD Ryzen Threadripper PRO 3995WX 64-Core CPUs running at 2.70 GHz. The numbers of elements, velocity and pressure DoFs are averaged values when AMR is used. The CPU time is the total accumulated time over the entire simulation.

		Elements	Velocity DoFs	Pressure DoFs	CPU time (seconds)
$Re = 2 \times 10^4$	Single-level	262,144	4,724,738	2,362,369	10,032
	AMR	27,940	540,104	270,052	2,049
$Re = 10^5$	Single-level	1,048,576	18,886,658	9,443,329	88,604
	AMR	66,665	1,275,076	637,538	8,302

difference between the single-level snapshots and their AMR counterparts. A close-up view of the vorticity field and the adaptive mesh is also shown in Figure 2, demonstrating the effectiveness of our adaptive solver. We have also implemented the UPPE formulation (21) and found that the L^2 -norm of the velocity divergence remains around 10^{-1} , leading to qualitatively incorrect results.

We also compare the performance of AMR to that of a single-level mesh in Table 6, where the four-level AMR hierarchy uses far fewer computational resources than the single-level mesh; for example, at $Re = 2 \times 10^4$ and $Re = 10^5$, the average number of elements in AMR is only 10.7% and 6.36% of that in the single-level mesh, respectively; the average number of pressure DoFs in AMR is only 11.4% and 6.75% of that in the single-level mesh, respectively, and the CPU time consumed by AMR is only 20.4% and 9.37% of that consumed by the single-level mesh, respectively. This clearly illustrates that AMR is very promising in simulating high-Reynolds-number flows. However, the relative savings of AMR on computational resources depend drastically on problem-specific aspects such as the refinement criteria and the number of levels. Hence the reader should not regard the results in Table 6 as universal estimates but rather just as one particular example of the efficiency of AMR.

4.2.2. Lid-driven cavity at $Re = 10^4$

This test examines the well-known 2D lid-driven cavity flow [50, 51], which undergoes a Hopf bifurcation from steady to unsteady periodic flow at a critical Reynolds number $Re_c \in [8017.6, 8018.8)$ [52]. We focus on a high Reynolds number of $Re = 10^4$, where the flow exhibits unsteady periodic behavior with multiple dominant frequencies [53]. The computational domain is the unit square $(0, 1)^2$, with the top lid moving horizontally at a constant velocity $U = 1$ to drive the flow, while the other three walls remain stationary. The simulation begins with an impulsive start, i.e., $\mathbf{u}_0 = \mathbf{0}$, and the forcing term is set to $\mathbf{f} = \mathbf{0}$.

The parameters in this test are as follows. The time span $[0, 500]$ is chosen sufficiently long to ensure the flow reaches a fully developed periodic state. After every 50 time steps, we adaptively refine and coarsen the mesh and adjust the time step size, where the number of refinements of the unit square $(0, 1)^2$ is allowed to vary between 6 and 8, and the thresholds for refinement and coarsening in the Dörfler marking strategy (42) are $\theta_R = 0.6$ and $\theta_C = 0.1$, respectively. The time step size is adjusted by (39) with a Courant number of $Cr = 1.2$.

The results of GePUP-FEM at the final time $t_e = 500$ are presented in Figure 3. The velocity profiles along the cavity centerlines (i.e., $u(0.5, y)$ and $v(x, 0.5)$) show excellent agreement with the benchmark data from Ghia et al. [50] and Erturk et al. [51], particularly in the boundary layer regions near the walls. Table 7 lists the maximum and minimum horizontal velocity values and their corresponding locations along the cavity centerline. Our results fall within the range of those reported by Ghia et al. [50] and Erturk et al. [51]. This test further demonstrates the capability of GePUP-FEM in accurately and efficiently resolving the underlying physics of high-Reynolds-number flows.

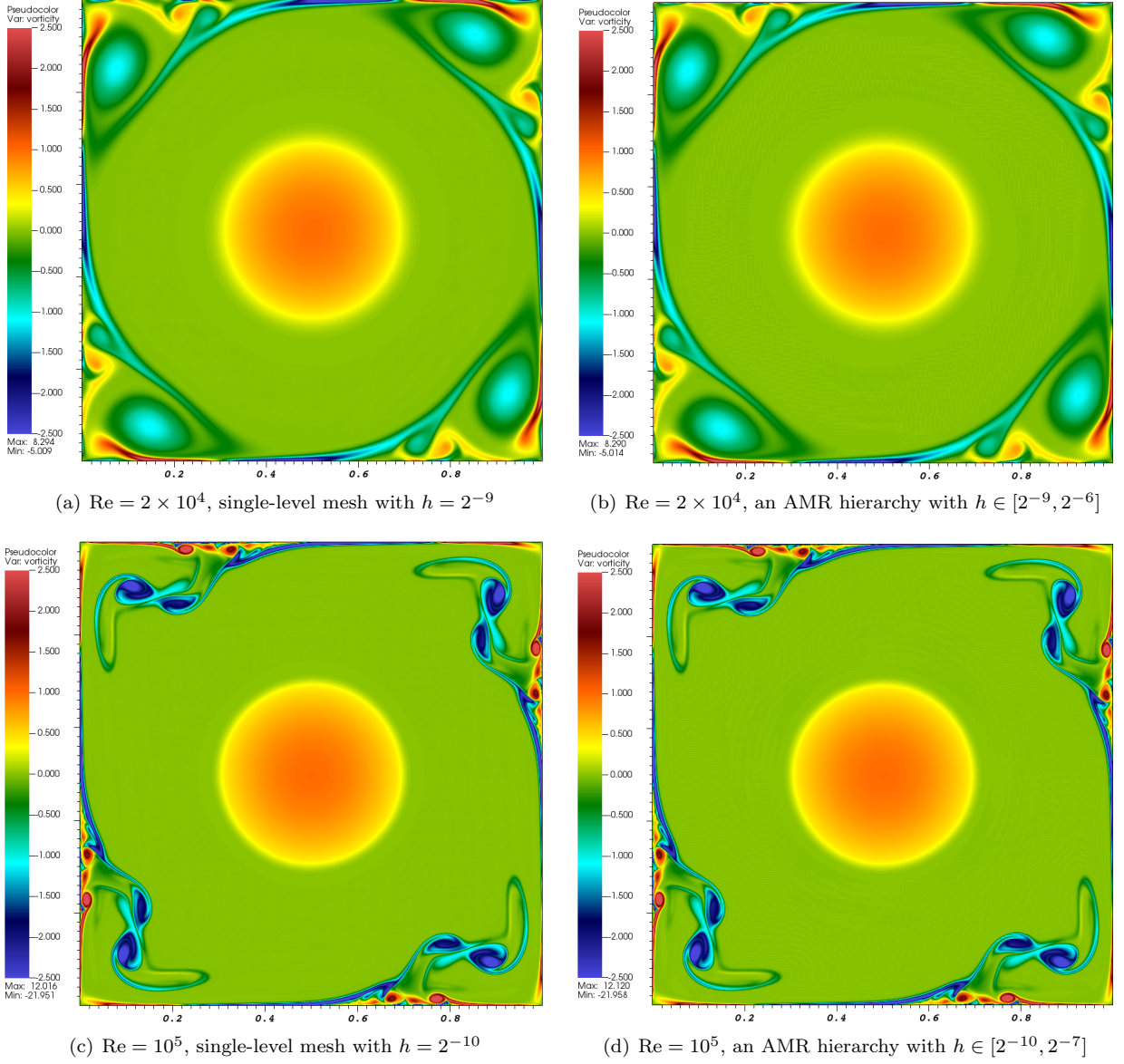


Figure 1: Results of GePUP-FEM of the vorticity field at $t_e = 60$ for the single-vortex test.

Table 7: Maximum and minimum horizontal velocity values and their corresponding x -coordinates along the cavity centerline for the lid-driven cavity flow at $Re = 10^4$ and $t = 500$.

	x_{\max}	v_{\max}	x_{\min}	v_{\min}
Ghia et al. [50]	0.063	0.4398	0.970	-0.5430
Erturk et al. [51]	0.060	0.4566	0.970	-0.5712
Present	0.061	0.4516	0.969	-0.5664

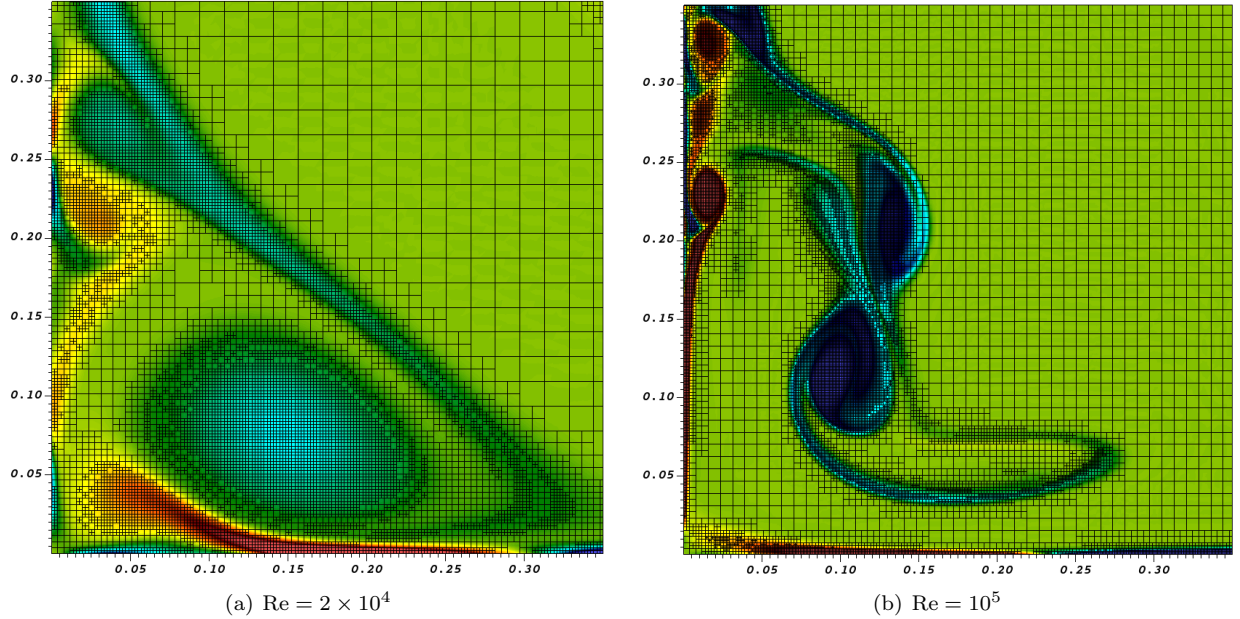


Figure 2: The vorticity field of GePUP-FEM at $t_e = 60$ on the locally refined mesh within $(0, 0.35)^2$ for the single-vortex test.

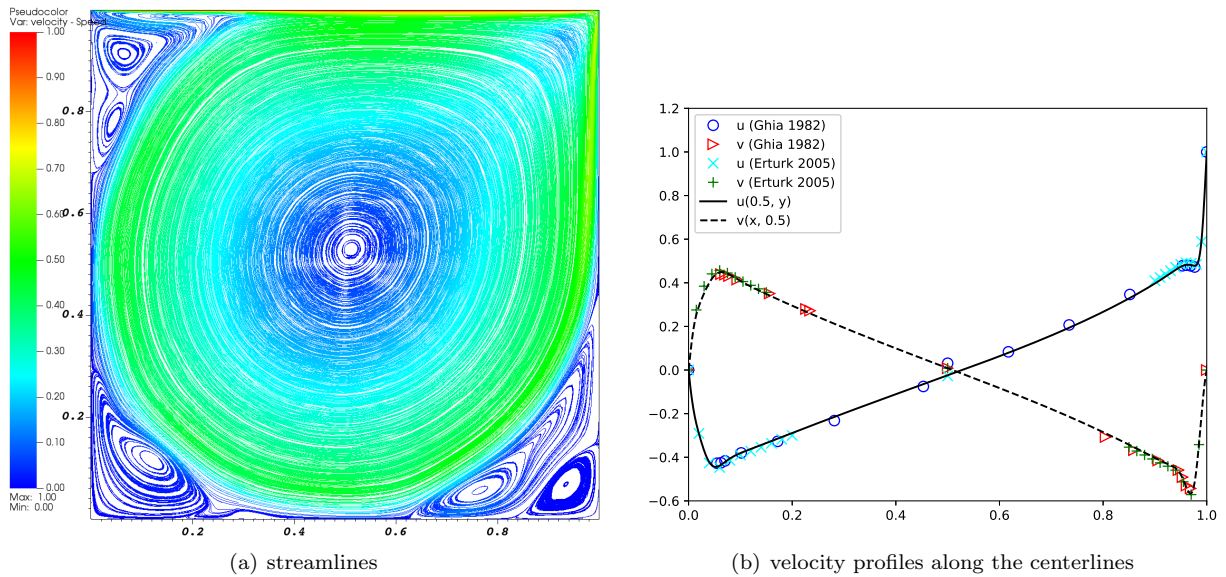


Figure 3: Results of GePUP-FEM for the lid-driven cavity flow at $Re = 10^4$ and $t = 500$.

4.2.3. Flow past a circular cylinder

In this test, we consider the popular benchmark of laminar flows past a circular cylinder, where the flow characteristics depend primarily on the Reynolds number. Experimental studies and numerical simulations [54] indicate that up to a Reynolds number (based on the freestream velocity and the cylinder diameter) of about 49 the flow is steady and symmetric with respect to the wake centerline. For higher Reynolds numbers, the flow becomes unsteady and exhibits periodic von Karman vortex shedding, exerting oscillatory drag and lift forces on the cylinder. The flow remains two-dimensional up to a Reynolds number of about 190, beyond which the flow becomes intrinsically three-dimensional.

The problem setup consists of a rectangular channel $(0, 32) \times (0, 16)$ containing a circular cylinder of diameter $D = 1$ centered at $(8, 8)$. On the left, top, and bottom walls, we impose for the velocity the Dirichlet boundary conditions

$$\mathbf{u}(x, y, t) = (U_\infty \omega(t), 0)^T, \quad U_\infty = 1, \quad \omega(t) = \begin{cases} \frac{1}{2} - \frac{1}{2} \cos(5\pi t) & t \leq \frac{1}{5}, \\ 1 & t > \frac{1}{5}, \end{cases}$$

where $\omega(t)$ regularizes the startup phase of the flow. On the cylinder surface, no-slip boundary conditions $\mathbf{u} = \mathbf{0}$ are enforced for the velocity, whereas on the right wall, homogeneous Neumann and homogeneous Dirichlet boundary conditions are enforced for the velocity \mathbf{u} and the pressure p , respectively. There is no external force, i.e., $\mathbf{f} = \mathbf{0}$. The density is set to $\rho = 1$ and the kinematic viscosity ν is chosen so that the Reynolds number $\text{Re} = U_\infty D / \nu$ is either 100 or 200.

For the right boundary of the domain, we impose the outflow condition by modifying boundary conditions in the GePUP formulation (28) as follows:

- for the momentum equation (28a), the condition of \mathbf{w} is homogeneous Neumann on the outflow boundary;
- for the projection equation (28c), we impose on ϕ homogeneous Dirichlet boundary conditions on the outflow boundary (so that the tangential velocity is preserved) and homogeneous Neumann boundary conditions on other walls (so that the normal velocity is preserved);
- for the pressure extraction equation (28e), we impose on q homogeneous Dirichlet boundary conditions on the outflow boundary and the Neumann boundary condition (28f) on other walls.

The parameters in this test are as follows. The time span is $[0, 200]$. After every 30 time steps, we adaptively refine and coarsen the mesh and adjust the time step size, where the thresholds for refinement and coarsening in the Dörfler marking strategy (42) are $\theta_R = 0.6$ ($\text{Re} = 100$), $\theta_R = 0.8$ ($\text{Re} = 200$), and $\theta_C = 0.1$. The time step size is adjusted by (39) and $\text{Cr} = 1.2$. To avoid a very small time step size caused by excessive mesh refinements, the initial mesh is refined at most r_{\max} times.

Snapshots of the vorticity field on the locally refined mesh within the subdomain $(6, 32) \times (5, 11)$ are shown in Figure 4, which clearly reveals the von Karman vortex street phenomenon for both $\text{Re} = 100$ and $\text{Re} = 200$. Refining the mesh with $r_{\max} = 3$ results in a mesh resolution of about $0.03D$ in the vicinity of the cylinder. During the periodic shedding of vortices, the number of pressure DoFs is approximately 4.7×10^4 , whereas refining every element in the initial mesh three times would increase the number of pressure DoFs to 305,472! This clearly illustrates how AMR algorithms can substantially reduce the problem size, thereby enhancing computational efficiency.

To validate our numerical solver against established results in the literature, we calculate the drag and lift coefficients, $C_D(t)$ and $C_L(t)$, obtained by evaluating the x - and y -components of the surface integral

$$\frac{2}{\rho U_\infty^2 D} \int_S (-q \mathbf{I} + 2\mu \boldsymbol{\sigma}) \mathbf{n},$$

where S is the surface of the cylinder, \mathbf{I} the identity tensor, $\mu = \rho \nu$ the dynamic viscosity, $\boldsymbol{\sigma} = (\nabla \mathbf{u} + \nabla \mathbf{u}^T) / 2$ the symmetric stress tensor, and \mathbf{n} the unit outward normal to the cylinder. We also calculate the dimensionless Strouhal number $\text{St} = f D / U_\infty$, where f is the vortex shedding frequency computed from the temporal variation of the lift coefficient $C_L(t)$.

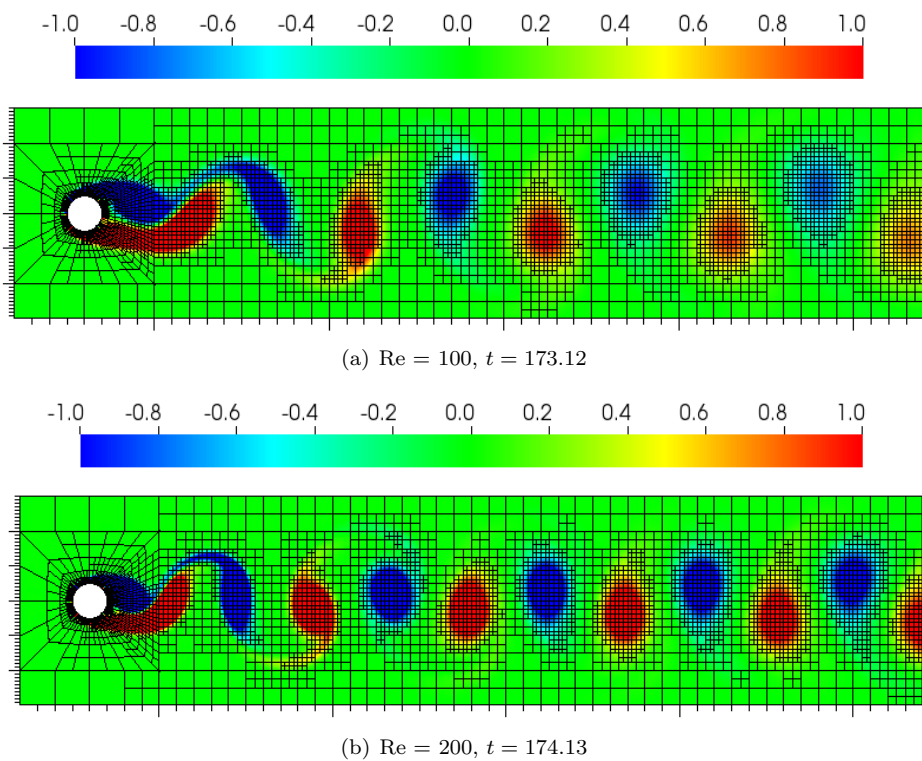


Figure 4: Snapshots of the vorticity field on the locally refined mesh within the subdomain $(6, 32) \times (5, 11)$ for the flow past a cylinder. The initial mesh is refined at most $r_{\max} = 3$ times.

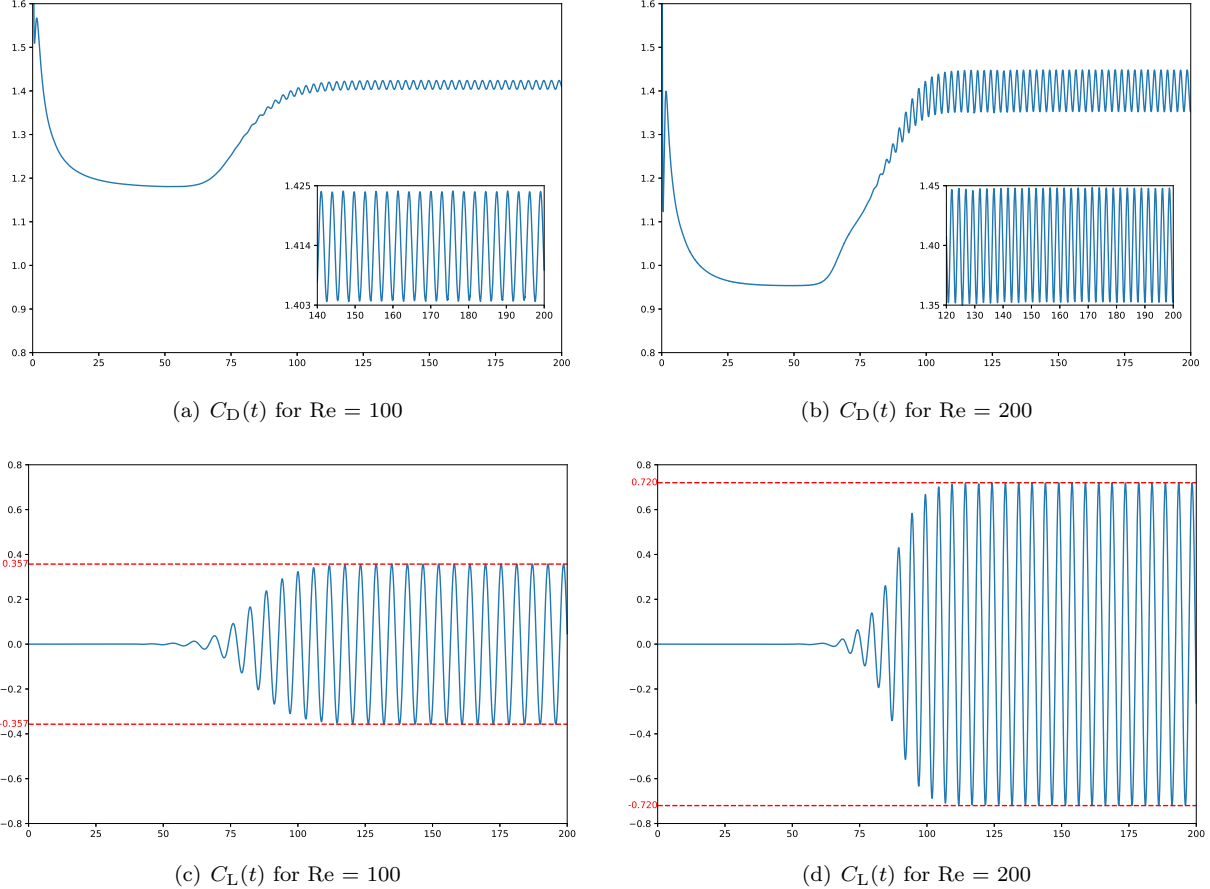


Figure 5: Temporal variations of the drag and lift coefficients for the flow past a circular cylinder. The abscissa represents time while an ordinate is the calculated value of a coefficient. The initial mesh is refined at most $r_{\max} = 4$ times. The results for $r_{\max} = 3$ are similar except that the vortex shedding occurs at a later time.

Temporal variations of the drag and lift coefficients for Reynolds numbers $Re = 100$ and $Re = 200$ are shown in Figure 5. For the higher Reynolds number, vortex shedding emerges earlier in the wake behind the cylinder and stabilizes into the Karman vortex street sooner. In Table 8, we list values of the drag coefficient, lift coefficient, and Strouhal number, demonstrating good agreements of our results with those in the literature.

4.2.4. Flow past a sphere

In this last test, we consider a more challenging benchmark of three-dimensional flows past a sphere. Similar to the flow past a circular cylinder, fully three-dimensional unsteady flow fields are generated from small perturbations despite the symmetry of the geometric configuration. Furthermore, these three-dimensional flows can exhibit even more intricate kinematic and vortical structures. Much like the circular cylinder case, the flow demonstrates several distinct regimes and the transition between those regimes depends on the Reynolds number. At Reynolds numbers (based on the freestream velocity and the diameter of the sphere) between 20 and approximately 210, the flow remains separated, steady, axisymmetric, and topologically similar, whereas the flow at Reynolds numbers between 210 and 270 is steady but non-axisymmetric. The onset of unsteadiness occurs at a Reynolds number in the range of 270 to 300, where the flow pattern exhibits periodic vortex shedding [61, 62, 63].

The problem setup is similar to that in Section 4.2.3. We consider a static sphere of diameter $D = 1$

Table 8: Drag coefficient, lift coefficient, and Strouhal number for the flow past a circular cylinder. The results for $r_{\max} = 5$ are identical to those for $r_{\max} = 4$ up to the displayed digits.

	Drag coefficient		Lift coefficient		Strouhal number	
	Re = 100	Re = 200	Re = 100	Re = 200	Re = 100	Re = 200
Blomquist et al. [16]	1.387 ± 0.019	1.370 ± 0.060	± 0.346	± 0.762	-	-
Braza et al. [55]	1.364 ± 0.015	1.400 ± 0.050	± 0.250	± 0.750	0.16	0.20
Liu et al. [56]	1.350 ± 0.012	1.310 ± 0.049	± 0.339	± 0.690	0.165	0.192
Kolahdouz et al. [57]	1.370 ± 0.015	1.390 ± 0.060	± 0.351	± 0.750	0.168	0.198
Calhoun [58]	1.330 ± 0.014	1.172 ± 0.058	± 0.298	± 0.668	0.175	0.202
Mahír et al. [59]	1.368 ± 0.029	1.376 ± 0.048	± 0.343	± 0.698	0.172	0.192
Xu et al. [60]	1.423 ± 0.013	1.420 ± 0.040	± 0.340	± 0.660	0.171	0.202
Present ($r_{\max} = 3$)	1.418 ± 0.011	1.402 ± 0.048	± 0.356	± 0.718	0.172	0.202
Present ($r_{\max} = 4$)	1.414 ± 0.011	1.400 ± 0.050	± 0.357	± 0.720	0.172	0.202

centered at $(8, 8, 8)$ within the rectangular box $(0, 32) \times (0, 16) \times (0, 16)$. On the left, top, bottom, front, and back walls, we impose for the velocity the Dirichlet boundary conditions

$$\mathbf{u}(x, y, z, t) = (U_{\infty}\omega(t), 0, 0)^T, \quad U_{\infty} = 1, \quad \omega(t) = \begin{cases} \frac{1}{2} - \frac{1}{2} \cos(5\pi t) & t \leq \frac{1}{5}, \\ 1 & t > \frac{1}{5}. \end{cases}$$

On the sphere surface, no-slip boundary conditions $\mathbf{u} = \mathbf{0}$ are enforced for the velocity, whereas on the right wall, homogeneous Neumann and homogeneous Dirichlet boundary conditions are enforced for the velocity \mathbf{u} and the pressure p , respectively. There is no external force, i.e., $\mathbf{f} = \mathbf{0}$. The density is set to $\rho = 1$ and the kinematic viscosity ν is deduced from the Reynolds number $\text{Re} = U_{\infty}D/\nu$, which, in this test, varies from 100 to 500, covering the different laminar flow regimes outlined above. The outflow boundary condition is implemented in the same manner as that in the third paragraph of Section 4.2.3.

The parameters for this test are as follows. The time span is $[0, 400]$. After every 50 time steps, we adaptively refine and coarsen the mesh and adjust the time step size, where the thresholds for refinement and coarsening in the Dörfler marking strategy (42) are $\theta_R = 0.6$ ($\text{Re} = 300$), $\theta_R = 0.7$ ($\text{Re} = 350$), $\theta_R = 0.8$ ($\text{Re} = 500$), and $\theta_C = 0.1$. The time step size is adjusted by (39) and $\text{Cr} = 0.8$. The initial mesh is refined at most $r_{\max} = 3$ times. The resulting mesh resolution in the vicinity of the sphere is approximately $0.078D$. For $\text{Re} = 500$, the number of DoFs for the pressure and the velocity is approximately 3×10^6 and 9×10^6 , respectively, which correspond to 2.62% of the number of DoFs for a uniform refinement of the initial mesh by three times.

To visualize vortical structures, we employ the Q-criterion [64] defined by

$$Q := \frac{1}{2} (\|\boldsymbol{\Omega}\|_2^2 - \|\boldsymbol{\sigma}\|_2^2), \quad (43)$$

where $\boldsymbol{\Omega} = (\nabla \mathbf{u} - \nabla \mathbf{u}^T)/2$ is the vorticity tensor, $\boldsymbol{\sigma}$ is the symmetric stress tensor, and $\|\cdot\|_2$ denotes the Frobenius norm. A vortex can be identified as the region surrounded by an isosurface of $Q > 0$, i.e., a region where the Frobenius norm of the vorticity tensor dominates that of the symmetric stress tensor.

Snapshots of the vortical structures for the unsteady flows at $\text{Re} = 300$ and $\text{Re} = 350$ are shown in Figure 6, where one clearly observes periodical shedding of harpin vortices from the sphere, the ubiquity of vortex loops in the wake, and the spanwise symmetry with respect to a vertical plane. These results are consistent with those reported in [61, 63], implying that the three-dimensional vortical structures have been successfully captured by GePUP-FEM.

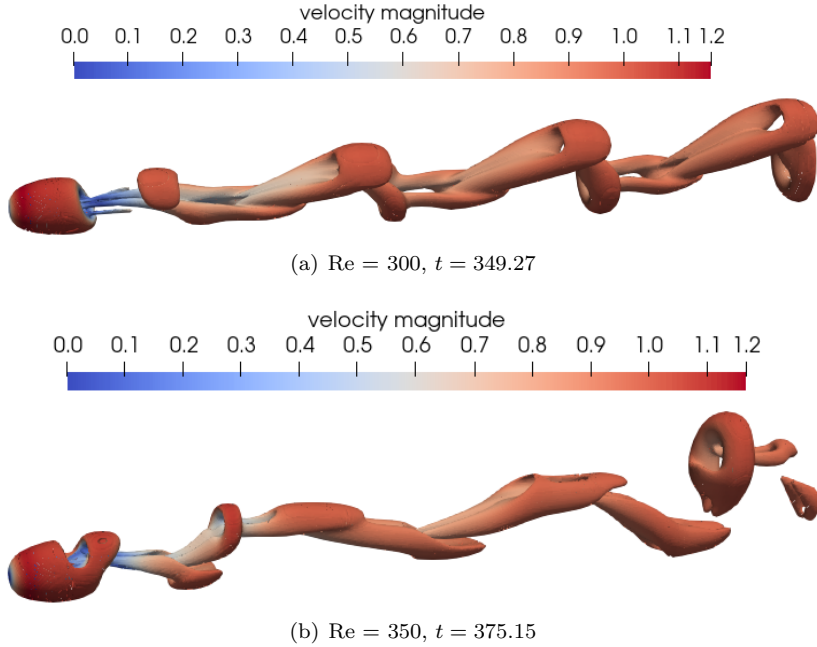


Figure 6: Instantaneous vortical structures identified by the Q-criterion (43) for the unsteady flow past a sphere. Isocontours of the Q-criterion ($Q = 0.001$) colored by the velocity magnitude are shown.

As in the previous test, we also evaluate the nondimensional force over the static sphere

$$\mathbf{F} = \frac{8}{\rho U_\infty^2 \pi D^2} \int_S (-q\mathbf{I} + 2\mu\boldsymbol{\sigma})\mathbf{n},$$

where S is the surface of the sphere and \mathbf{n} the unit outward normal to the sphere. The drag coefficient $C_D(t)$ and the lift coefficients $C_L(t)$, $C_{L,y}(t)$, $C_{L,z}(t)$ are defined by

$$C_D(t) = \mathbf{F} \cdot \mathbf{e}_x, \quad C_L(t) = \sqrt{C_{L,y}(t)^2 + C_{L,z}(t)^2}, \quad C_{L,y}(t) = \mathbf{F} \cdot \mathbf{e}_y, \quad C_{L,z}(t) = \mathbf{F} \cdot \mathbf{e}_z.$$

Due to the axisymmetry of the flow at $Re = 100$ and $Re = 200$, the lift coefficient $C_L(t)$ should be identically zero [61]. Our numerical results are 3.86×10^{-13} and 8.91×10^{-5} , both being close to zero. The temporal variations of the drag coefficient $C_D(t)$ and the lift coefficients $C_{L,y}(t)$ and $C_{L,z}(t)$ at Reynolds numbers 250, 300, 350, and 500 are shown in Figure 7. The lift coefficients $C_{L,y}(t)$ and $C_{L,z}(t)$ at $Re = 250$ approach nonzero constants after a nondimensional time of approximately $tU_\infty/D = 150$; this is consistent with the experimental observation that the flow is non-axisymmetric but remains steady. At $Re = 300$ and $Re = 350$, the flow is unsteady and vortices periodically shed from the static sphere [65, 66]. We evaluate the Strouhal number $St = fD/U_\infty$, where the vortex shedding frequency f is obtained by calculating the averaged period between successive peak values in the temporal variation of the lift coefficient $C_{L,z}(t)$.

Our numerical results of the Strouhal number and the averaged drag coefficient $C_D(t)$ and the averaged lift coefficient $C_L(t)$ within the time interval $[200, 400]$ are summarized and compared with available data from the literature in Tables 9 and 10. Our results agree well with those in previous studies, confirming the accuracy of GePUP-FEM over a relatively wide range of Reynolds numbers.

5. Conclusion

We have presented GePUP-FEM, high-order finite element methods for solving the incompressible Navier-Stokes equations. The weak form of the GePUP formulation is first derived and high-order GePUP-FEM schemes with method-of-lines are then proposed. Results of standard benchmark problems show

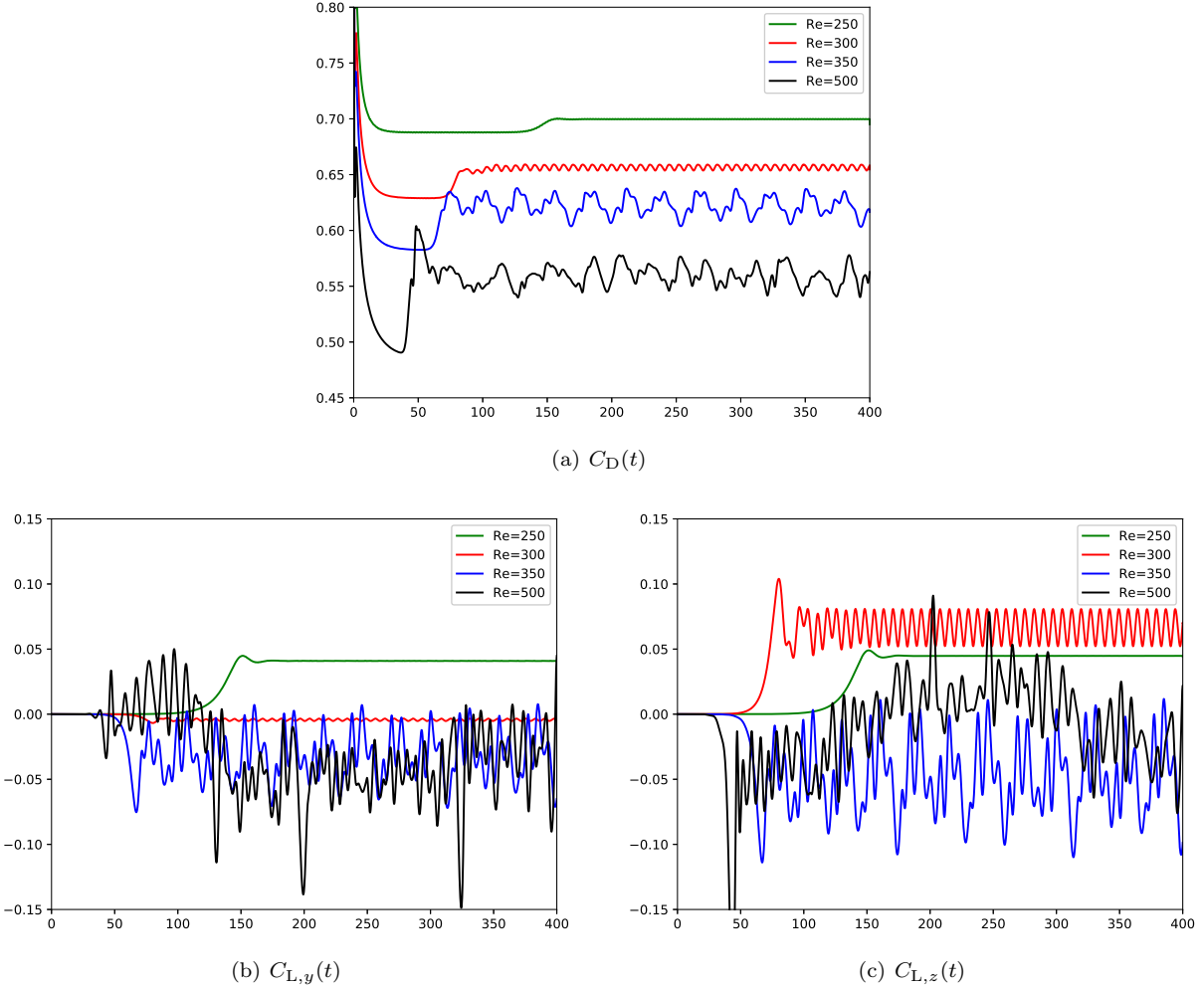


Figure 7: Temporal variations of the drag and lift coefficients for the flow past a sphere. The abscissa represents time while an ordinate is the calculated value of a coefficient.

Table 9: Values of the averaged drag coefficient within $t \in [200, 400]$ for the flow past a sphere.

	Re = 100	Re = 200	Re = 250	Re = 300	Re = 350	Re = 500
Blomquist et al. [16]	1.058	0.768	-	0.646	0.601	-
Johnson et al. [61]	1.08	0.78	0.70	0.656	-	-
Bagchi et al. [65]	1.09	-	0.70	-	0.62	0.555
Mittal et al. [66]	1.08	-	-	0.67	0.625	-
Constantinescu et al. [67]	-	-	0.70	0.655	-	-
Kim et al. [68]	1.087	-	0.701	0.657	-	-
Hartmann et al. [69]	1.083	0.764	0.698	0.657	-	-
Giacobello et al. [70]	-	-	0.702	0.658	-	-
Present ($r_{\max} = 2$)	1.071	0.765	0.699	0.657	0.622	0.558
Present ($r_{\max} = 3$)	1.080	0.767	0.700	0.657	0.622	0.560

Table 10: Values of the averaged lift coefficient within $t \in [200, 400]$ and the Strouhal number for the flow past a sphere.

	Lift coefficient		Strouhal number	
	Re = 250	Re = 300	Re = 300	Re = 350
Johnson et al. [61]	0.062	0.069	0.137	-
Bagchi et al. [65]	-	-	-	0.135
Mittal et al. [66]	-	-	0.135	0.142
Constantinescu et al. [67]	0.062	0.065	0.136	-
Kim et al. [68]	0.059	0.067	0.134	-
Hartmann et al. [69]	0.065	0.069	0.135	-
Giacobello et al. [70]	0.061	0.067	0.134	-
Present ($r_{\max} = 2$)	0.060	0.066	0.134	0.136
Present ($r_{\max} = 3$)	0.061	0.067	0.134	0.133

that GePUP-FEM not only achieves high-order accuracy both in time and in space, but is also capable of accurately and efficiently resolving the right physics. Furthermore, GePUP-FEM offers the flexibility of choosing finite element spaces for the velocity and the pressure so that the algorithmic steps can be free of the standard inf-sup condition.

A number of future research prospects follow. To further enhance the stability and robustness of GePUP-FEM in simulating flows with high Reynolds numbers, we can employ some stabilization techniques, such as continuous interior penalty [71], where a penalty term on the jump of the gradient over element boundaries is added. To better guide the adaptive mesh refinement process, rigorous a posteriori error estimates need to be established [72]. We also plan to generalize GePUP-FEM to simulate flows with moving boundaries, such as those in [73] and [74], via incorporating high-order interface tracking methods [75, 76] and unfitted Eulerian finite element methods [77, 78].

Acknowledgments

We are grateful to two anonymous referees for their insightful comments and valuable suggestions. This work was supported by the grant 12272346 from the National Natural Science Foundation of China.

References

- [1] C. L. Fefferman, Existence and smoothness of the Navier-Stokes equation, in: J. Carlson, A. Jaffe, A. Wiles (Eds.), *The Millennium Prize Problems*, American Mathematical Society, Providence, Rhode Island, 2006, pp. 57–67.
- [2] S. Smale, Mathematical problems for the next century, *Math. Intelligencer* 20 (2) (1998) 7–15.
- [3] K. Devlin, *The Millennium Problems: The Seven Greatest Unsolved Mathematical Puzzles of Our Time*, Basic Books, New York, 2003.
- [4] Q. Zhang, GePUP: Generic projection and unconstrained PPE for fourth-order solutions of the incompressible Navier-Stokes equations with no-slip boundary conditions, *J. Sci. Comput.* 67 (3) (2016) 1134–1180.
- [5] D. Boffi, F. Brezzi, M. Fortin, *Mixed Finite Element Methods and Applications*, Springer-Verlag, Berlin Heidelberg, 2013.
- [6] E. Burman, M. A. Fernández, Continuous interior penalty finite element method for the time-dependent Navier-Stokes equations: space discretization and convergence, *Numer. Math.* 107 (2007) 39–77.
- [7] R. Codina, J. Principe, O. Guasch, S. Badia, Time dependent subscales in the stabilized finite element approximation of incompressible flow problems, *Comput. Methods Appl. Mech. Engrg.* 196 (21) (2007) 2413–2430.
- [8] M. Benzi, G. H. Golub, J. Liesen, Numerical solution of saddle point problems, *Acta Numer.* 14 (2005) 1–137.
- [9] A. J. Chorin, Numerical solution of the Navier-Stokes equations, *Math. Comp.* 22 (104) (1968) 745–762.
- [10] R. Temam, Sur l’approximation de la solution des équations de Navier-Stokes par la méthode des pas fractionnaires II, *Arch. Ration. Mech. Anal.* 33 (1969) 377–385.
- [11] D. L. Brown, R. Cortez, M. L. Minion, Accurate projection methods for the incompressible Navier-Stokes equations, *J. Comput. Phys.* 168 (2) (2001) 464–499.

- [12] J. L. Guermond, P. Minev, J. Shen, An overview of projection methods for incompressible flows, *Comput. Methods Appl. Mech. Engrg.* 195 (44-47) (2006) 6011–6045.
- [13] L. H. Howell, J. B. Bell, An adaptive mesh projection method for viscous incompressible flow, *SIAM J. Sci. Comput.* 18 (4) (1997) 996–1013.
- [14] D. F. Martin, P. Colella, D. Graves, A cell-centered adaptive projection method for the incompressible Navier-Stokes equations in three dimensions, *J. Comput. Phys.* 227 (3) (2008) 1863–1886.
- [15] D. Trebotich, D. T. Graves, An adaptive finite volume method for the incompressible Navier-Stokes equations in complex geometries, *Commun. Appl. Math. Comput. Sci.* 10 (1) (2015) 43–82.
- [16] M. Blomquist, S. R. West, A. L. Binswanger, M. Theillard, Stable nodal projection method on octree grids, *J. Comput. Phys.* 499 (2024) 112695.
- [17] J. B. Bell, P. Colella, H. M. Glaz, A second-order projection method for the incompressible Navier-Stokes equations, *J. Comput. Phys.* 85 (2) (1989) 257–283.
- [18] J. Kim, P. Moin, Application of a fractional-step method to incompressible Navier-Stokes equations, *J. Comput. Phys.* 59 (2) (1985) 308–323.
- [19] P. M. Gresho, R. L. Sani, On pressure boundary conditions for the incompressible Navier-Stokes equations, *Int. J. Numer. Methods Fluids* 7 (10) (1987) 1111–1145.
- [20] B. Sanderse, B. Koren, Accuracy analysis of explicit Runge-Kutta methods applied to the incompressible Navier-Stokes equations, *J. Comput. Phys.* 231 (8) (2012) 3041–3063.
- [21] H. Johnston, J.-G. Liu, Accurate, stable and efficient Navier-Stokes solvers based on explicit treatment of the pressure term, *J. Comput. Phys.* 199 (1) (2004) 221–259.
- [22] J.-G. Liu, J. Liu, R. L. Pego, Stability and convergence of efficient Navier-Stokes solvers via a commutator estimate, *Comm. Pure Appl. Math.* 60 (10) (2007) 1443–1487.
- [23] J.-G. Liu, J. Liu, R. L. Pego, Error estimates for finite-element Navier-Stokes solvers without standard inf-sup conditions, *Chinese Ann. Math. Ser. B* 30 (6) (2009) 743–768.
- [24] J. Liu, Open and traction boundary conditions for the incompressible Navier-Stokes equations, *J. Comput. Phys.* 228 (19) (2009) 7250–7267.
- [25] J.-G. Liu, J. Liu, R. L. Pego, Stable and accurate pressure approximation for unsteady incompressible viscous flow, *J. Comput. Phys.* 229 (9) (2010) 3428–3453.
- [26] J. Jia, J. Liu, Stable and spectrally accurate schemes for the Navier-Stokes equations, *SIAM J. Sci. Comput.* 33 (5) (2011) 2421–2439.
- [27] D. Shirokoff, R. R. Rosales, An efficient method for the incompressible Navier-Stokes equations on irregular domains with no-slip boundary conditions, high order up to the boundary, *J. Comput. Phys.* 230 (23) (2011) 8619–8646.
- [28] R. R. Rosales, B. Seibold, D. Shirokoff, D. Zhou, High-order finite element methods for a pressure Poisson equation reformulation of the Navier-Stokes equations with electric boundary conditions, *Comput. Methods Appl. Mech. Engrg.* 373 (2021) 113451.
- [29] G. E. Karniadakis, M. Israeli, S. A. Orszag, High-order splitting methods for the incompressible Navier-Stokes equations, *J. Comput. Phys.* 97 (2) (1991) 414–443.
- [30] N. A. Petersson, Stability of pressure boundary conditions for Stokes and Navier-Stokes equations, *J. Comput. Phys.* 172 (1) (2001) 40–70.
- [31] E. Leriche, E. Perchat, G. Labrosse, M. O. Deville, Numerical evaluation of the accuracy and stability properties of high-order direct Stokes solvers with or without temporal splitting, *J. Sci. Comput.* 26 (1) (2006) 25–43.
- [32] L. Li, A split-step finite-element method for incompressible Navier-Stokes equations with high-order accuracy up-to the boundary, *J. Comput. Phys.* 408 (2020) 109274.
- [33] F. Meng, J. W. Banks, W. D. Henshaw, D. W. Schwendeman, Fourth-order accurate fractional-step IMEX schemes for the incompressible Navier-Stokes equations on moving overlapping grids, *Comput. Methods Appl. Mech. Engrg.* 366 (2020) 113040.
- [34] D. R. Q. Pacheco, R. Schussnig, T.-P. Fries, An efficient split-step framework for non-Newtonian incompressible flow problems with consistent pressure boundary conditions, *Comput. Methods Appl. Mech. Engrg.* 382 (2021) 113888.
- [35] U. M. Ascher, S. J. Ruuth, R. J. Spiteri, Implicit-explicit Runge-Kutta methods for time-dependent partial differential equations, *Appl. Numer. Math.* 25 (2) (1997) 151–167.
- [36] C. A. Kennedy, M. H. Carpenter, Additive Runge-Kutta schemes for convection-diffusion-reaction equations, *Appl. Numer. Math.* 44 (1) (2003) 139–181.
- [37] C. A. Kennedy, M. H. Carpenter, Higher-order additive Runge-Kutta schemes for ordinary differential equations, *Appl. Numer. Math.* 136 (2019) 183–205.
- [38] D. Arndt, W. Bangerth, D. Davydov, T. Heister, L. Heltai, M. Kronbichler, M. Maier, J.-P. Pelteret, B. Turcksin, D. Wells, The **DEAL.II** finite element library: Design, features, and insights, *Comput. Math. Appl.* 81 (2021) 407–422.
- [39] C. Burstedde, L. C. Wilcox, O. Ghatsas, **p4est**: Scalable algorithms for parallel adaptive mesh refinement on forests of octrees, *SIAM J. Sci. Comput.* 33 (3) (2011) 1103–1133.
- [40] M. Kronbichler, K. Kormann, A generic interface for parallel cell-based finite element operator application, *Comput. & Fluids* 63 (2012) 135–147.
- [41] W. Bangerth, C. Burstedde, T. Heister, M. Kronbichler, Algorithms and data structures for massively parallel generic adaptive finite element codes, *ACM Trans. Math. Software* 38 (2) (2011) 14:1–14:28.
- [42] T. C. Clevenger, T. Heister, G. Kanschat, M. Kronbichler, A flexible, parallel, adaptive geometric multigrid method for FEM, *ACM Trans. Math. Software* 47 (1) (2020) 7:1–7:27.
- [43] G. I. Taylor, A. E. Green, Mechanism of the production of small eddies from large ones, *Proc. R. Soc. Lond. Ser. A, Math.*

Phys. Sci. 158 (895) (1937) 499–521.

[44] N. C. Nguyen, J. Peraire, B. Cockburn, An implicit high-order hybridizable discontinuous Galerkin method for the incompressible Navier–Stokes equations, *J. Comput. Phys.* 230 (4) (2011) 1147–1170.

[45] C. R. Ethier, D. A. Steinman, Exact fully 3D Navier–Stokes solutions for benchmarking, *Int. J. Numer. Methods Fluids* 19 (5) (1994) 369–375.

[46] M. Piatkowski, S. Müthing, P. Bastian, A stable and high-order accurate discontinuous Galerkin based splitting method for the incompressible Navier–Stokes equations, *J. Comput. Phys.* 356 (2018) 220–239.

[47] W. Dörfler, A convergent adaptive algorithm for Poisson’s equation, *SIAM J. Numer. Anal.* 33 (3) (1996) 1106–1124.

[48] C.-M. Pfeiler, D. Praetorius, Dörfler marking with minimal cardinality is a linear complexity problem, *Math. Comp.* 89 (326) (2020) 2735–2752.

[49] J. B. Bell, P. Colella, L. H. Howell, An efficient second-order projection method for viscous incompressible flow, in: AIAA 10th Computational Fluid Dynamics Conference, Honolulu, Hawaii, June 24–26, 1991, pp. 360–367.

[50] U. Ghia, K. N. Ghia, C. T. Shin, High-Re solutions for incompressible flow using the Navier–Stokes equations and a multigrid method, *J. Comput. Phys.* 48 (3) (1982) 387–411.

[51] E. Erturk, T. C. Corke, C. Gökçöl, Numerical solutions of 2-D steady incompressible driven cavity flow at high Reynolds numbers, *Int. J. Numer. Methods Fluids* 48 (7) (2005) 747–774.

[52] F. Auteri, N. Parolini, L. Quartapelle, Numerical investigation on the stability of singular driven cavity flow, *J. Comput. Phys.* 183 (1) (2002) 1–25.

[53] C.-H. Bruneau, M. Saad, The 2D lid-driven cavity problem revisited, *Comput. & Fluids* 35 (3) (2006) 326–348.

[54] C. H. K. Williamson, Vortex dynamics in the cylinder wake, *Annu. Rev. Fluid Mech.* 28 (1996) 477–539.

[55] M. Braza, P. Chassaing, H. H. Minh, Numerical study and physical analysis of the pressure and velocity fields in the near wake of a circular cylinder, *J. Fluid Mech.* 165 (1986) 79–130.

[56] C. Liu, X. Zheng, C. H. Sung, Preconditioned multigrid methods for unsteady incompressible flows, *J. Comput. Phys.* 139 (1) (1998) 35–57.

[57] E. M. Kolahdouz, A. P. S. Bhalla, B. A. Craven, B. E. Griffith, An immersed interface method for discrete surfaces, *J. Comput. Phys.* 400 (2020) 108854.

[58] D. Calhoun, A Cartesian grid method for solving the two-dimensional streamfunction-vorticity equations in irregular regions, *J. Comput. Phys.* 176 (2) (2002) 231–275.

[59] N. Mahír, Z. Altaç, Numerical investigation of convective heat transfer in unsteady flow past two cylinders in tandem arrangements, *Int. J. Heat Fluid Flow* 29 (5) (2008) 1309–1318.

[60] S. Xu, Z. J. Wang, An immersed interface method for simulating the interaction of a fluid with moving boundaries, *J. Comput. Phys.* 216 (2) (2006) 454–493.

[61] T. A. Johnson, V. C. Patel, Flow past a sphere up to a Reynolds number of 300, *J. Fluid Mech.* 378 (1999) 19–70.

[62] D. Ormières, M. Provansal, Transition to turbulence in the wake of a sphere, *Phys. Rev. Lett.* 83 (1) (1999) 80–83.

[63] A. G. Tomboulides, S. A. Orszag, Numerical investigation of transitional and weak turbulent flow past a sphere, *J. Fluid Mech.* 416 (2000) 45–73.

[64] J. C. R. Hunt, A. A. Wray, P. Moin, Eddies, streams, and convergence zones in turbulent flows, *Proceedings of the Summer Program, Center for Turbulence Research, Stanford University* (1988).

[65] P. Bagchi, M. Y. Ha, S. Balachandar, Direct numerical simulation of flow and heat transfer from a sphere in a uniform cross-flow, *J. Fluids Eng.* 123 (2) (2001) 347–358.

[66] R. Mittal, H. Dong, M. Bozkurttas, F. M. Najjar, A. Vargas, A. von Loebbecke, A versatile sharp interface immersed boundary method for incompressible flows with complex boundaries, *J. Comput. Phys.* 227 (10) (2008) 4825–4852.

[67] G. S. Constantinescu, K. D. Squires, LES and DES investigations of turbulent flow over a sphere at $Re = 10,000$, *Flow Turbul. Combust.* 70 (1–4) (2003) 267–298.

[68] J. Kim, D. Kim, H. Choi, An immersed-boundary finite-volume method for simulations of flow in complex geometries, *J. Comput. Phys.* 171 (1) (2001) 132–150.

[69] D. Hartmann, M. Meinke, W. Schröder, A strictly conservative Cartesian cut-cell method for compressible viscous flows on adaptive grids, *Comput. Methods Appl. Mech. Engrg.* 200 (9) (2011) 1038–1052.

[70] M. Giacobello, A. Ooi, S. Balachandar, Wake structure of a transversely rotating sphere at moderate Reynolds numbers, *J. Fluid Mech.* 621 (2009) 103–130.

[71] E. Burman, D. Garg, J. Guzman, Implicit-explicit time discretization for Oseen’s equation at high Reynolds number with application to fractional step methods, *SIAM J. Numer. Anal.* 61 (6) (2023) 2859–2886.

[72] E. Bänsch, A. Brenner, A posteriori error estimates for pressure-correction schemes, *SIAM J. Numer. Anal.* 54 (4) (2016) 2323–2358.

[73] S. Gross, A. Reusken, *Numerical Methods for Two-phase Incompressible Flows*, Springer-Verlag, Berlin Heidelberg, 2011.

[74] T. Richter, *Fluid-structure Interactions: Models, Analysis and Finite Elements*, Springer, Cham, 2017.

[75] Q. Zhang, A. Fogelson, MARS: An analytic framework of interface tracking via mapping and adjusting regular semi-algebraic sets, *SIAM J. Numer. Anal.* 54 (2) (2016) 530–560.

[76] Q. Zhang, Fourth- and higher-order interface tracking via mapping and adjusting regular semianalytic sets represented by cubic splines, *SIAM J. Sci. Comput.* 40 (6) (2018) A3755–A3788.

[77] E. Burman, S. Claus, P. Hansbo, M. G. Larson, A. Massing, CutFEM: Discretizing geometry and partial differential equations, *Int. J. Numer. Meth. Engng.* 104 (7) (2015) 472–501.

[78] C. Lehrenfeld, M. Olshanskii, An Eulerian finite element method for PDEs in time-dependent domains, *ESAIM Math. Model. Numer. Anal.* 53 (2) (2019) 585–614.